https://doi.org/10.5194/egusphere-2026-6527
Preprint. Discussion started: 4 November 2026
© Author(s) 2026. CC BY 4.0 License.

Silicon redistribution and promoted low-latitude diatom growth after Atlantic circulation recovered from deglacial meltwater discharge

Ying Ye[1], Peter Köhler[1], Martin Butzin[1], and Christoph Völker[1]

[1]Alfred-Wegener-Institut Helmholtz-Zentrum für Polar- und Meeresforschung (AWI), P.O. Box 12 01 61, 27515 Bremerhaven, Germany

Correspondence: Ying Ye (Ying.Ye@awi.de)

Abstract. How the marine silicon cycle modulates the biological carbon pump and contributes to glacial–interglacial variations in atmospheric CO_2 remains unresolved. Proposed mechanisms include Southern Ocean silicic acid leakage, stimulating low-latitude diatom productivity either during the Last Glacial Maximum (LGM) or at the onset of deglaciation, and deglacial silicon redistribution from the abyss to the surface. To test these hypotheses, we performed two equilibrium simulations (pre-industrial and LGM), one LGM sensitivity simulation with pre-industrial dust deposition and two freshwater perturbation experiments under LGM conditions with the Earth system model AWI-ESM2.1, in which the diatom silicon-to-nitrogen (Si:N) uptake ratio varies with the nutrient limitation state. Glacial dust deposition enriches Southern Ocean surface waters and southern-sourced intermediate waters in silicon relative to nitrogen, but strengthened stratification traps this reservoir, preventing it from fuelling low-latitude diatom growth. We identify two mechanisms that release silicon to low-latitude surface waters: (1) the recovery of the Atlantic Meridional Overturning Circulation (AMOC) after the freshwater perturbation strengthens intermediate-water formation, upwells the leaked silicon and drives short-lived but pronounced opal export peaks in the tropics; (2) continued warming and sea-ice retreat mobilise the deep glacial silicon pool, sustaining a more persistent enhancement. A longer freshwater perturbation suppresses the first mechanism. Despite some discrepancies in timing, our results reconcile previous hypotheses within a unified framework, defining circulation recovery as the critical trigger that links freshwater forcing to sedimentary opal records.

1 Introduction

It is now widely accepted that the ∼90 ppm glacial–interglacial variations in atmospheric CO_2 concentrations observed in the late Pleistocene (Marcott et al., 2014; Bereiter et al., 2015) cannot be attributed to a single mechanism, but rather result from a combination of processes – the so-called "carbon stew" (Kohfeld and Ridgwell, 2009; Ganopolski and Brovkin, 2017). Recent modelling studies incorporating deep-ocean radiocarbon data suggest that physical components of the marine carbon

https://doi.org/10.5194/egusphere-2026-6527
Preprint. Discussion started: 4 November 2026
© Author(s) 2026. CC BY 4.0 License.

pump may account for approximately two-thirds of these CO_2 changes (Skinner et al., 2023; Köhler et al., 2024), implying a significant role for biological processes in explaining the remaining variability.

Among the suggested processes driving the biological carbon pump, the Silicic Acid Leakage Hypothesis (SALH; Brzezinski et al., 2002; Matsumoto et al., 2002) has received particular attention, with sediment records providing both supporting and contradictory evidence over the past two decades. The SALH proposes that iron fertilisation from enhanced glacial dust deposition in the Southern Ocean (SO) reduces diatom silicon (Si) uptake relative to nitrogen (N), based on the observed higher Si:N ratios in diatoms under iron limitation (Marchetti and Cassar, 2009, and citations therein). This creates a Si excess in SO surface waters, which, if transported via Antarctic Intermediate Water (AAIW) or Sub-Antarctic Mode Water (SAMW) to low latitudes, could stimulate diatom growth there while suppressing the export of calcifying phytoplankton. While the soft-tissue pump might not be affected significantly, this mechanism would weaken the carbonate counter pump, contributing to glacial CO_2 drawdown. Matsumoto and Sarmiento (2008) proposed a corollary to the SALH, in which the competitive advantage of diatoms over calcifying phytoplankton, rather than the absolute amount of low-latitude diatom production, determines the effect on the carbonate counter pump. Atmospheric CO_2 could therefore decrease even with a reduced silicic acid supply to low latitudes, provided that the supplied waters have elevated Si:N ratios.

Si isotope data confirm reduced Si utilisation in the glacial SO (de La Rocha et al., 1998; Beucher et al., 2007), while coupled δ^{30}Si and δ^{15}N studies reveal Si-enriched subantarctic surface waters during the Last Glacial Maximum (LGM) (Beucher et al., 2007; Horn et al., 2011). However, low-latitude opal flux reconstructions show regional inconsistencies in diatom productivity responses to Si leakage. Figure 1a, b and e synthesise equatorial opal accumulation rates from published data sets (see Fig. A1 for individual records). In the central and eastern equatorial Pacific most cores show similar or lower opal fluxes during the LGM compared to the Holocene, with only a few cores exhibiting higher opal accumulation at the LGM, resulting in a similar overall distribution between the two periods (Fig. 1e). In contrast, most cores from the equatorial Atlantic demonstrate higher opal accumulation during the LGM than in the Holocene, with distinct deglacial peaks (Figs. 1b and A1b, c).

The divergent patterns in the tropical Atlantic and Pacific indicate dynamic nutrient redistribution across climate states, driven by physical transport. The Silicic Acid Ventilation Hypothesis (SAVH; Hendry and Brzezinski, 2014) reconciles the LGM and deglacial sediment records by attributing the absence of increased opal fluxes at low latitudes during the LGM to enhanced stratification and reduced upwelling, while linking the deglacial rise in Si supply and diatom productivity to abrupt changes in upwelling and mixing during Heinrich Stadial 1 (HS1). Recent work based on Si isotopes in the SO has led to a further scenario, the Abyssal Silicon Hypothesis (ASH; Dumont et al., 2020). This suggests that, despite the increased SO overturning during HS1, the deep ocean remained stratified, trapping dissolved silicon (DSi) within the lower overturning cell. Only when the Younger Dryas began, a continued loss of sea ice and a southward shift in the westerlies facilitated enhanced deep mixing, triggering a massive redistribution of DSi from the abyss via intermediate waters to the surface waters at lower latitudes.

Earth system models allow the response of the climate system to a single, controlled perturbation to be isolated. In this study we employ the Earth system model AWI-ESM2.1, which includes a marine carbon cycle component (REcoM3p) with a variable diatom Si:N ratio regulated by nutrient limitation, to test these hypotheses and to investigate the mechanisms during the LGM

https://doi.org/10.5194/egusphere-2026-6527
Preprint. Discussion started: 4 November 2026
© Author(s) 2026. CC BY 4.0 License.

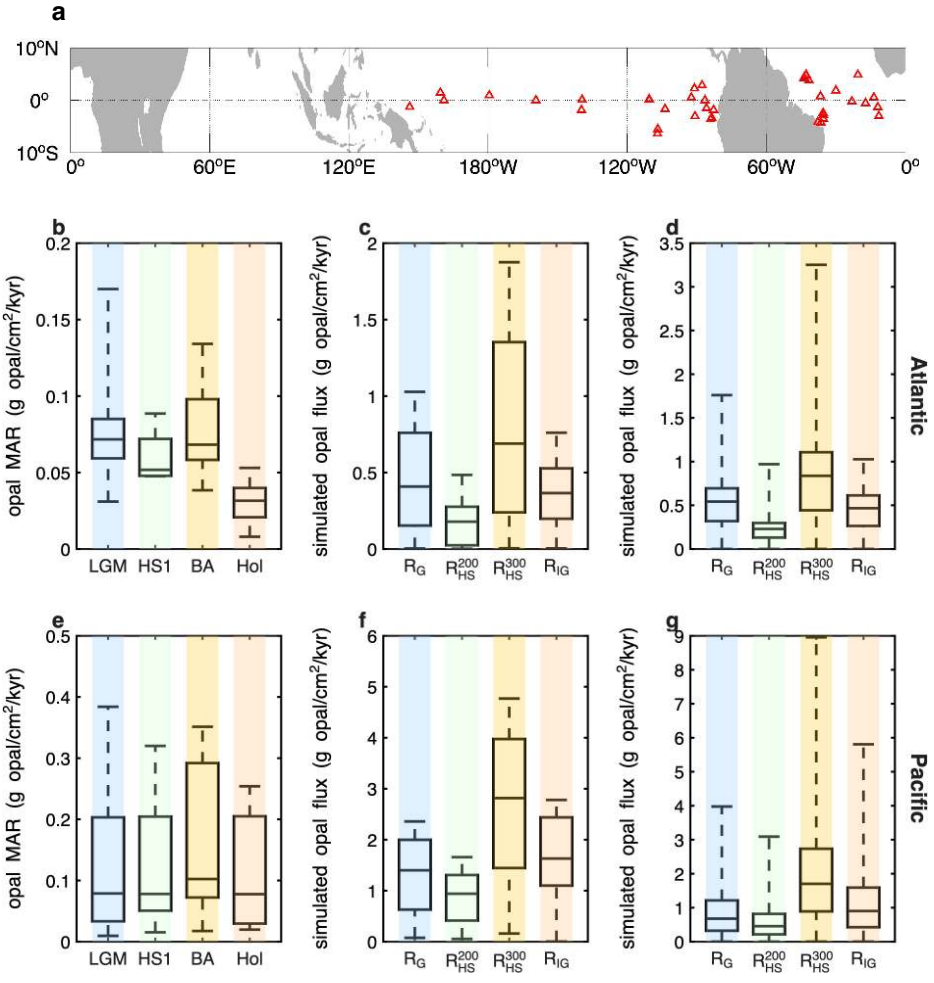


Figure 1. Reconstructed marine opal accumulation rates from 24 kyr BP to present (Bradtmiller et al., 2006, 2007; Kienast et al., 2006; Richaud et al., 2007; Pichevin et al., 2009; Dubois et al., 2010; Lippold et al., 2012), compared with simulated opal fluxes to the seafloor. **(a)** Locations of cores used for panels (b) and (e). **(b, e)** Reconstructed opal mass accumulation rates (MAR) in the equatorial Atlantic (b) and Pacific (e) for the Last Glacial Maximum (LGM; 23–19 ka), Heinrich Stadial 1 (HS1; 18–14.7 ka), Bølling–Allerød (BA; 14.7–12.9 ka) and the late Holocene (Hol; 4.2–0 ka); see Sect. 2.4 for how the statistics were computed. **(c, f)** Simulated opal flux to the sediments at the corresponding core locations in the equatorial Atlantic (c) and Pacific (f) for simulations R_G, R_{HS}^{200}, R_{HS}^{300} and R_{IG}. Boxes show the 0.25–0.75 quantiles, whiskers the full range, and horizontal lines the medians. The superscript X in R_{HS}^{X} denotes the simulated year. **(d, g)** As (c) and (f) but averaged over the equatorial Atlantic (d) and Pacific (g) (5° S–5° N). Simulated opal fluxes to the sediment surface (rain) are compared with reconstructed opal burial fluxes, showing an approximately one-order-of-magnitude offset, consistent with the estimated ratio between the global biogenic Si flux delivered to sediments and its net burial (Tréguer et al., 2021).

https://doi.org/10.5194/egusphere-2026-6527
Preprint. Discussion started: 4 November 2026
© Author(s) 2026. CC BY 4.0 License.

and the onset of deglaciation that may have affected the transport of Si to low latitudes and its upwelling there, thereby altering the marine biological carbon pumps. In addition to a pre-industrial and an LGM simulation, we use a sensitivity simulation with pre-industrial dust deposition under LGM climate to demonstrate the effect of glacial dust deposition, and two freshwater-perturbation experiments to examine how freshwater-induced circulation changes redistribute Si, and when and through which pathways Si leaked from the Southern Ocean can reach low-latitude diatoms.

2 Methods

2.1 AWI-ESM2.1

We used the AWI Earth System Model (AWI-ESM2.1; Ackermann et al., 2024; Shi et al., 2023), an Earth system model developed at the Alfred Wegener Institute (AWI). Model components are the atmospheric model ECHAM6 (Stevens et al., 2013) in its T63L47 setup with approximately 1.9° horizontal resolution and 47 vertical layers; the land vegetation and hydrology model JSBACH3.2 (Raddatz et al., 2007); and the Finite-volumE Sea ice-Ocean Model FESOM2.1 (Danilov et al., 2017; Sidorenko et al., 2019), which uses unstructured meshes that enable locally increased resolution. The ocean mesh used in this study has a resolution of about 100 km in the open ocean, 25 km over polar areas and 35 km along coastlines (Koldunov et al., 2019; Scholz et al., 2022). AWI-ESM2.1 has been used to simulate the LGM within the Paleoclimate Modelling Intercomparison Project Phase 4 (PMIP4); its physical LGM state has been evaluated against palaeoclimate reconstructions and lies within the range of the PMIP4 models (Kageyama et al., 2021). Another detailed evaluation of the physical state of the LGM simulation is presented in Shi et al. (2025). For this study, AWI-ESM2.1 was extended with a marine biogeochemistry component, the Regulated Ecosystem Model REcoM3. REcoM3 and its coupling to FESOM2.1 have been described by Gürses et al. (2023). We use the configuration of REcoM3 for palaeo-applications, FESOM2.1-REcoM3p (Ye et al., 2025), with the setup of a one-layer sediment.

Atmospheric CO_2 concentrations are calculated assuming that the atmosphere can be represented as a homogeneous carbon reservoir, determined by the globally integrated air–sea CO_2 flux (Ye et al., 2025). Changes in the carbon cycle on land are not considered. This atmospheric CO_2 box therefore only serves to quantify the impact of the marine carbon pumps on atmospheric CO_2, while the radiative forcing is regulated by prescribing greenhouse gases from reconstructions.

2.2 Diatoms in REcoM3

REcoM3 describes cycles of carbon, oxygen and nutrients (nitrogen, silicon and iron) with varying intracellular stoichiometry in phytoplankton, zooplankton and detritus. Two phytoplankton groups are considered in REcoM3p: diatoms and small phytoplankton including calcifiers. Growth of both groups is controlled by light, temperature and nutrients including dissolved inorganic nitrogen (DIN) and dissolved iron (DFe), while that of diatoms depends additionally on DSi. Diatoms have higher Si:N and Si:C cellular ratios when growing under iron-depleted conditions, which might be caused by changes in morphology (reduction of cell size or increase of Si-containing valve surface area relative to volume) (Marchetti and Harrison, 2007;

https://doi.org/10.5194/egusphere-2026-6527
Preprint. Discussion started: 4 November 2026
© Author(s) 2026. CC BY 4.0 License.

Marchetti and Cassar, 2009) or by the degree of silicification (Takeda, 1998). This phenomenon is represented in REcoM3 by the decoupling of N and Si assimilation under strong nutrient limitation, following Claquin et al. (2002). N assimilation by diatoms ($V^{\mathrm{N}}_{\mathrm{dia}}$) is a function of the maximum photosynthesis rate ($P^{\mathrm{dia}}_{\mathrm{max}}$), the intracellular N:C quota ($Q^{\mathrm{N:C}}_{\mathrm{dia}}$) and the external DIN concentration as a Michaelis–Menten term (Eq. 1), where $K^{\mathrm{N}}_{\mathrm{dia}}$ is the half-saturation constant for diatom DIN uptake. Here, $P^{\mathrm{dia}}_{\mathrm{max}}$ is regulated by temperature and by the most limiting nutrient among DIN, DSi and DFe according to Liebig's law of the minimum. The limitation factor f_{lim} is determined by a quota approach, depending on the deviation between the intracellular nutrient quota and a prescribed maximum quota ($Q^{\mathrm{N:C}}_{\mathrm{dia,max}}$). Limitation factors by DSi and DFe are determined based on Michaelis–Menten kinetics in a similar way to DIN.

$$V^{\mathrm{N}}_{\mathrm{dia}} = P^{\mathrm{dia}}_{\mathrm{max}} \cdot f_{\mathrm{lim}}\left(\theta, Q^{\mathrm{N:C}}_{\mathrm{dia}}, Q^{\mathrm{N:C}}_{\mathrm{dia,max}}\right) \cdot \frac{\mathrm{DIN}}{K^{\mathrm{N}}_{\mathrm{dia}} + \mathrm{DIN}} \tag{1}$$

Si assimilation is calculated in a similar way but without the regulation by the most limiting nutrient. Under strong nutrient limitation, e.g. by iron, Si uptake only depends on DSi availability and the intracellular Si quota, while N uptake additionally depends on the availability of DFe, leading to higher Si:N ratios in diatoms. This parameterisation of diatom physiology therefore allows us to test the SALH, starting from the premise that enhanced dust deposition over the SO results in lower Si:N utilisation by diatoms and a Si excess in surface waters.

2.3 Experimental design

Five simulations were carried out (Table 1): a pre-industrial (PI) or interglacial (IG) control run (R_{IG}), a glacial (G) or LGM run (R_G), a sensitivity run under LGM climate with PI dust deposition ($R_{G\text{-}PIdust}$), and two experiments in which freshwater is added to the North Atlantic (NA) for different durations under LGM boundary conditions (R_{HS} and R_{HL} for short and long freshwater hosing, respectively).

Simulations were forced by the respective orbital parameters (Berger and Loutre, 1991) and greenhouse gas concentrations following the PMIP4 protocol (PI: 284.3 ppm CO_2, 808.2 ppb CH_4 and 273.0 ppb N_2O; LGM: 190 ppm CO_2, 375 ppb CH_4 and 200 ppb N_2O; Kageyama et al., 2017), which determine radiative forcing. The land–sea mask, ice sheets and topography are prescribed according to the GLAC-1D reconstruction (Tarasov et al., 2012). Dust input of iron at the sea surface is calculated from monthly averages of simulated dust deposition for the PI and LGM climate (Albani et al., 2014), with an iron content of 3.5 wt % and a solubility of 2 %.

R_{IG} and R_G were both initialised with January temperatures and salinities from the Polar Science Center Hydrographic Climatology (PHC3; Steele et al., 2001). For the mass conservation of carbon in the atmosphere–ocean system, the atmospheric CO_2 box in both simulations was initialised with the PI CO_2 concentration. In R_{IG}, alkalinity and dissolved inorganic carbon (DIC) were initialised from version 2 of the Global Ocean Data Analysis Project (GLODAPv2) data set (Lauvset et al., 2016), DIN and DSi from the World Ocean Atlas 2013 (Garcia et al., 2014), and oxygen from the World Ocean Atlas 2018 (Garcia et al., 2019). The initial DFe field is based on output from the Pelagic Interaction Scheme for Carbon and Ecosystem Studies (PISCES) model (Aumont et al., 2015). In R_G, the water-column inventories of DIC, alkalinity, DIN, DSi and oxygen are kept

https://doi.org/10.5194/egusphere-2026-6527
Preprint. Discussion started: 4 November 2026
© Author(s) 2026. CC BY 4.0 License.

Table 1. Overview of the simulations. All simulations use AWI-ESM2.1 with FESOM2.1-REcoM3p. $R_{G\text{-}PIdust}$, R_{HS} and R_{HL} were initialised from the end of R_G. GHG: greenhouse gases.

Simulation	Boundary conditions	Freshwater forcing	Length (years)	Analysis period
R_{IG}	PI orbit GHG (CO_2 284.3 ppm, CH_4 808.2 ppb, N_2O 273.0 ppb) PI ice sheets PI dust	none	1500	last 50 years
R_G	LGM orbit GHG (CO_2 190 ppm, CH_4 375 ppb, N_2O 200 ppb) GLAC-1D ice sheets LGM dust	none	1500	last 50 years
$R_{G\text{-}PIdust}$	as R_G, but PI dust	none	300	last 50 years
R_{HS}	as R_G	0.2 Sv, 50–70° N in the Atlantic, years 1–250	1300	10-year means at key stages
R_{HL}	as R_G	0.2 Sv, 50–70° N in the Atlantic, years 1–500	1300	10-year means at key stages

https://doi.org/10.5194/egusphere-2026-6527
Preprint. Discussion started: 4 November 2026
© Author(s) 2026. CC BY 4.0 License.

identical to R_{IG} by increasing concentrations by 3 %, corresponding to the lower sea level. R_{IG} and R_G were run for 1500 model years to reach equilibrium in the deep ocean. The last 50 years of both simulations were averaged for analysis.

R_{HS} and R_{HL} were initialised with the final state of R_G and run for another 1300 years. Freshwater was added between 50 and 70° N over the entire width of the NA at the same rate (0.2 Sv) in R_{HS} for 250 years and in R_{HL} for 500 years. The end of the hosing period represents the cessation of iceberg discharge. R_{HS} was designed to produce a weakening of the Atlantic Meridional Overturning Circulation (AMOC) of a magnitude comparable to that inferred for HS1 (Pöppelmeier et al., 2023). R_{HL} is not intended to represent a specific event but tests the robustness of the results from R_{HS} under a different freshwater perturbation magnitude and duration. Because all other boundary conditions are kept at LGM values, R_{HS} and R_{HL} are idealised experiments that isolate the circulation-driven response of nutrient redistribution and atmospheric CO_2.

To demonstrate the effect of glacial dust deposition on the SO Si excess, an additional simulation ($R_{G\text{-}PIdust}$) was initialised from the end of R_G and run for 300 years with PI dust deposition (Albani et al., 2014), as in R_{IG}, under otherwise unchanged LGM boundary conditions. The last 50 years were averaged for analysis.

Table 2. Key stages selected from the freshwater-perturbation experiments. Each stage is analysed as a 10-year mean ending at the given model year.

Phase	R_{HS}	R_{HL}	Characteristics
Weak-AMOC phase	year 200	year 400	AMOC reduced to ∼5 Sv; reduced tropical opal flux
Recovered-AMOC phase	year 300	year 600	AMOC recovered after the end of hosing; first tropical opal peak in R_{HS}, none in R_{HL}
Stabilised AMOC	year 600	year 1000	AMOC stabilised; slight opal enhancement in the tropical Atlantic
Progressive-warming phase	year 1000	year 1200	opal enhancement in both the tropical Atlantic and Pacific

We analysed the temporal evolution of R_{HS} and R_{HL} and selected characteristic key stages, each distinguished by a different state of the AMOC and of the opal flux (Table 2). Simulated opal fluxes were examined at 100-year intervals throughout both experiments to ensure that no major features were missed between the selected stages. A 10-year mean was computed over the period ending at each respective year. In the following, we refer to the stages by the simulated year (e.g. R_{HS}^{200}) and by the phase names in Table 2; the phase names describe the circulation state in the experiments.

2.4 Opal compilation and model–data comparison

For comparison with the model results, we compiled published opal accumulation rates from the equatorial Atlantic and Pacific (Bradtmiller et al., 2006, 2007; Kienast et al., 2006; Richaud et al., 2007; Pichevin et al., 2009; Dubois et al., 2010; Lippold et al., 2012), either taken directly from the publications or calculated from opal content, sedimentation rate and dry bulk density. For cores published with different age models, only the most recent version was retained. The records are provided in Tables S1 (Atlantic) and S2 (Pacific) in the Supplement, and core locations are shown in Fig. 1a.

https://doi.org/10.5194/egusphere-2026-6527
Preprint. Discussion started: 4 November 2026
© Author(s) 2026. CC BY 4.0 License.

The records were grouped into the LGM (23–19 ka), HS1 (18–14.7 ka), the Bølling–Allerød (BA; 14.7–12.9 ka) and the late Holocene (4.2–0 ka). For each interval and basin, all data of all cores falling into the interval are shown as box plots (median, 0.25–0.75 quantiles and full range; Fig. 1b, e).

Simulated opal fluxes were extracted at the core locations and averaged over the equatorial band (5° S–5° N) of each basin. The model simulates the opal flux onto the sediment but not its burial. Since more than 90 % of the opal flux redissolves at the sediment–water interface (Tréguer and De La Rocha, 2013; Tréguer et al., 2021), simulated fluxes are about an order of magnitude higher than reconstructed accumulation rates, and the comparison focuses on relative changes between climate states. A point-to-point comparison requires precise agreement between the model and reality in the location of boundaries, such as fronts and upwelling zones. Comparisons based on signals integrated over entire regions, in turn, require sufficiently extensive spatial coverage of proxy data. Both requirements pose challenges when comparing a high-resolution global ocean model with a sparse proxy dataset. We therefore provide both comparisons (Fig. 1c, f and d, g).

3 Results

3.1 Glacial state and increased storage of C and Si in the deep ocean

This study focuses on the simulated glacial and interglacial marine silicon cycle and its impact on the carbon cycle. The physical LGM state of AWI-ESM2.1 has been evaluated within PMIP4 (Kageyama et al., 2021; Shi et al., 2025). In our simulations, the mean ocean temperature is 4.0 °C in R_{IG} and 1.87 °C in R_G, i.e. a glacial cooling of 2.13 °C, within the range of the estimate by Seltzer et al. (2024) (2.27±0.46 °C). Global mean sea surface temperature (SST) is 1.7 °C lower in R_G, within the reconstructed range of SST cooling of the MARGO project (Waelbroeck et al., 2009) but below the range of -3.4 to -2.9 °C of Tierney et al. (2020).

Comparing R_G and R_{IG}, the colder glacial ocean (Fig. A2b) stores more carbon, drawing down atmospheric CO_2 by 53 ppm. This additional carbon is primarily stored in the saltier and denser deep Pacific and in Antarctic Bottom Water (AABW) (Figs. A2a and A3a), resulting in a 6 % and 2 % increase in DIC in the deep Pacific and deep Atlantic (>3000 m), respectively. Similar to DIC, glacial DSi accumulates mainly in the deep Pacific and AABW (Fig. A3b). While our setup focuses on key drivers of the marine carbon cycle, other potential contributors to the CO_2 change are not considered, e.g. coral reef growth, volcanic outgassing and continental weathering (Kohfeld and Ridgwell, 2009; Ganopolski and Brovkin, 2017; Köhler and Munhoven, 2020; Wu et al., 2022), and the land carbon cycle is not represented. These omissions may explain the offset between the simulated and the reconstructed (∼90 ppm) glacial CO_2 anomaly.

3.2 Response of biological productivity to glacial climate conditions

Simulated total marine net primary production (NPP) in R_{IG} is 35.7 PgC yr^{-1}, close to results from previous ocean-only simulations with FESOM2.1-REcoM3 (Gürses et al., 2023; Ye et al., 2025). The global NPP in R_G does not differ significantly from that in R_{IG}; however, the relative contribution of the SO (south of 40° S) to global carbon export increases from 36 % to 41 %,

https://doi.org/10.5194/egusphere-2026-6527
Preprint. Discussion started: 4 November 2026
© Author(s) 2026. CC BY 4.0 License.

indicating a higher efficiency of the marine biological carbon pump despite larger glacial sea-ice cover. Indeed, the global transfer efficiency (calculated as the fraction of particulate organic carbon (POC) flux at 1000 m relative to that at 100 m) rises from 20 % under PI conditions to 25 % during the LGM. The global $CaCO_3$:POC export ratio shows a small increase during the LGM (Fig. A4), indicating little contribution of the carbonate counter pump to the glacial CO_2 drawdown.

Regional patterns (Fig. 2) reveal reduced glacial productivity in parts of the high latitudes in both hemispheres, driven by expanded sea ice and cooling. Decreased high-latitude nutrient utilisation, together with enhanced dust deposition (Fig. A5), promotes higher productivity between 30 and 60° in both hemispheres and in some upwelling regions during the LGM. These patterns compare well with the qualitative assessment of relative changes in export production (Kohfeld et al., 2005, 2013), except in some shelf regions that are not well resolved by our model configuration. A clear bimodal change emerges in the SO, with increases north of the Antarctic Polar Front (APF) and decreases to the south. This pattern is consistent with an equatorward, wind-driven displacement of the Antarctic Circumpolar Current (ACC) fronts and associated upwelling zones (Sigman et al., 2021) combined with enhanced glacial dust fertilisation.

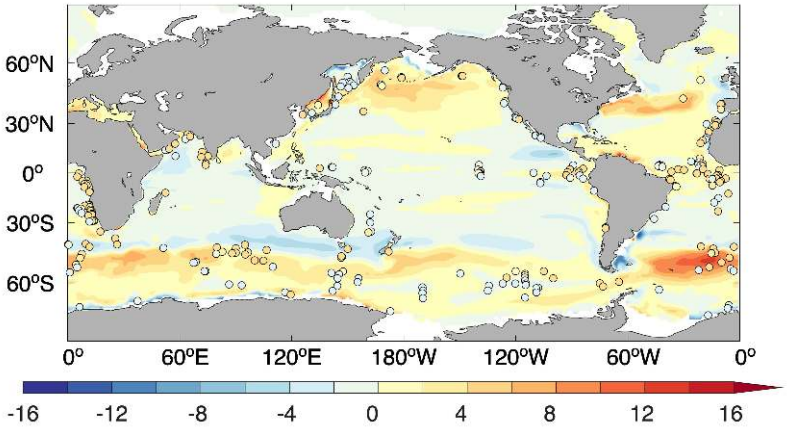


Figure 2. Simulated anomaly (R_G–R_{IG}) of particulate organic carbon export (mmol C m^{-2} d^{-1}) compared with qualitative estimates of the LGM–PI change in export production on a five-point scale from lower to higher export (Kohfeld et al., 2005, 2013; coloured circles).

3.3 Silicic acid leakage during the LGM

Cooling and extended sea ice (Figs. A2b and A6) weakened upwelling in the subantarctic ocean and reduced nutrient supply to the surface ocean, in accordance with sediment records (Bradtmiller et al., 2009; Beucher et al., 2007; Bostock et al., 2004). These effects, together with increased glacial dust deposition (Fig. A5), shifted diatom productivity and carbon deposition on the seafloor northward from ∼60° S to 40–50° S (Fig. 3a, b). At the same time, glacial opal deposition rates in the SO are largely lower than at PI (Fig. 3c). This negative anomaly occurs despite higher carbon export and diatom productivity between 40 and 50° S (Fig. 3a–c), reflecting a decoupling of the carbon and silicon cycles, mainly caused by the lower Si:N uptake ratio of diatoms in the iron-enriched glacial ocean. The negative anomalies in opal flux to the seafloor south of the APF are

https://doi.org/10.5194/egusphere-2026-6527
Preprint. Discussion started: 4 November 2026
© Author(s) 2026. CC BY 4.0 License.

consistent with sediment reconstructions (Bradtmiller et al., 2009; Chase et al., 2003). North of the APF, the model reproduces the positive anomaly in the Indian and Atlantic sectors (Frank et al., 2000) of the SO, as well as in the central and western Pacific sector (Bradtmiller et al., 2009), whereas a negative anomaly is simulated in the eastern Pacific sector, which does not agree with reconstructions (Bradtmiller et al., 2009). Given that the modelled diatom productivity captures the reconstructed north–south contrast across the APF (Fig. 3a), the mismatch of opal deposition in the eastern Pacific sector suggests that the Si:N ratio in the simulated export fluxes may be underestimated there, likely leading to an overestimation of the Si excess in SO surface waters potentially available for transport to lower latitudes. The lack of iron supply from iceberg melt in the model may lead to an underestimation of iron concentrations far north in the SO, which could also contribute to this mismatch.

The simulated response of Si:N ratios in diatoms to iron enrichment (Fig. 4e) is within the range of measurements in laboratory and field studies (Marchetti and Cassar, 2009). It leads to higher Si:N ratios in glacial SO surface waters between 40 and 50° S (Fig. 4f), where the glacial diatom belt is located and where the formation of glacial AAIW is shifted northward (Fig. A7a, b). This high-Si:N signature propagates northward at intermediate depths (Fig. 5a, b) and could potentially favour diatom growth in the tropics, as presumed by the SALH.

However, R_G shows only modest increases in diatom NPP and carbon deposition in the tropical upwelling regions, with opal deposition rising slightly in the equatorial Atlantic but decreasing in the equatorial Pacific (Figs. 1c, d, f, g and 3a–c). Averaged over the equatorial band (5° S–5° N), the simulated opal deposition changes by about 25 % in both basins, with opposite signs, which qualitatively agrees with the inter-basin contrast in the reconstructions (Fig. 1b, e). Low-latitude surface waters exhibit reduced DSi concentrations and Si:N ratios in R_G (Figs. A3b and A8b), indicating a limited influence of southern-sourced, high-Si:N waters.

This also holds for the community composition of export production, the quantity that matters in the corollary to the SALH (Matsumoto and Sarmiento, 2008). In the tropical ocean (5° S–5° N), the $CaCO_3$:POC export ratio increases from 0.062 in R_{IG} to 0.073 in R_G (Fig. A4). In our simulations, low-latitude export production therefore shifts slightly towards calcifiers rather than diatoms under glacial conditions, opposite to the prediction of the corollary, because neither the Si:N ratio nor the DSi concentration of low-latitude surface waters increases (Figs. A3b and A8a, b).

Indeed, the wind-driven upwelling of DSi between 5° S and 5° N in the tropical Pacific is lowered by 33 % in R_G compared to R_{IG} (Fig. 5c), limiting Si supply to the low-latitude surface waters and contributing to the lower opal deposition. This reduction is driven by small differences in wind stress and, more importantly, by enhanced upper-ocean stratification in R_G, which weakens vertical exchange with deeper nutrient-rich waters. The tropical Atlantic shows a more heterogeneous upwelling pattern, with substantially enhanced upwelling around 1° S and north of 2° N and reduced upwelling in adjacent regions (Fig. 5d), which helps explain the similar to slightly higher glacial opal deposition there.

Reconstructions also indicate that subantarctic surface waters were enriched in Si relative to N during the LGM, and that this Si-rich signature was primarily incorporated into SAMW and AAIW (Beucher et al., 2007). The absence of this Si enrichment in subtropical and tropical surface waters has been explained by lower rates of intermediate-water formation during glacial periods (Crosta et al., 2007). Our model results support this interpretation, showing weaker intermediate-water formation during the LGM (Fig. A7a, b), which reduces the equatorward transport of the Si excess.

https://doi.org/10.5194/egusphere-2026-6527
Preprint. Discussion started: 4 November 2026
© Author(s) 2026. CC BY 4.0 License.

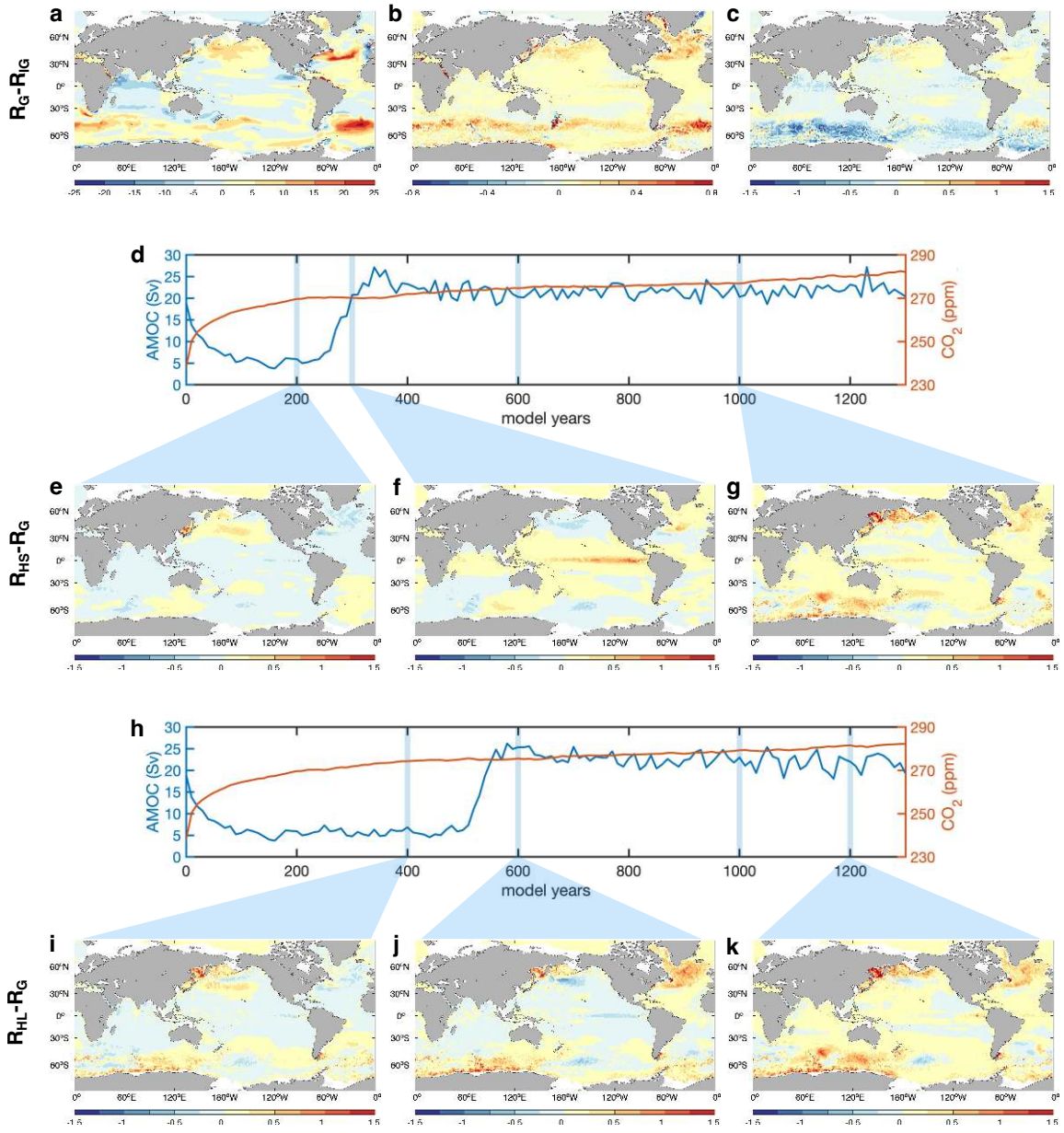


Figure 3. (a–c) Anomaly (R_G–R_{IG}) in (a) diatom NPP (mmol C m^{-2} d^{-1}), (b) POC deposition onto the sediment (mmol C m^{-2} d^{-1}) and (c) opal deposition onto the sediment (mmol Si m^{-2} d^{-1}). **(d)** Temporal evolution of the AMOC (Sv) and atmospheric CO_2 (ppm) in R_{HS}. **(e–g)** Anomaly (R_{HS}–R_G) in opal deposition onto the sediment (mmol Si m^{-2} d^{-1}) for the selected stages shown in (d): (e) year 200 with the weakest AMOC, (f) year 300 with the first opal peak in the tropics and (g) year 1000 with the second opal peak. **(h)** Temporal evolution of the AMOC (Sv) and atmospheric CO_2 (ppm) in R_{HL}. **(i–k)** Anomaly (R_{HL}–R_G) in opal deposition onto the sediment for the selected stages shown in (h): (i) year 400, (j) year 600 and (k) year 1200, which captures the only opal peak in this experiment. Key stages (Table 2) are indicated with solid blue bars.

https://doi.org/10.5194/egusphere-2026-6527
Preprint. Discussion started: 4 November 2026
© Author(s) 2026. CC BY 4.0 License.

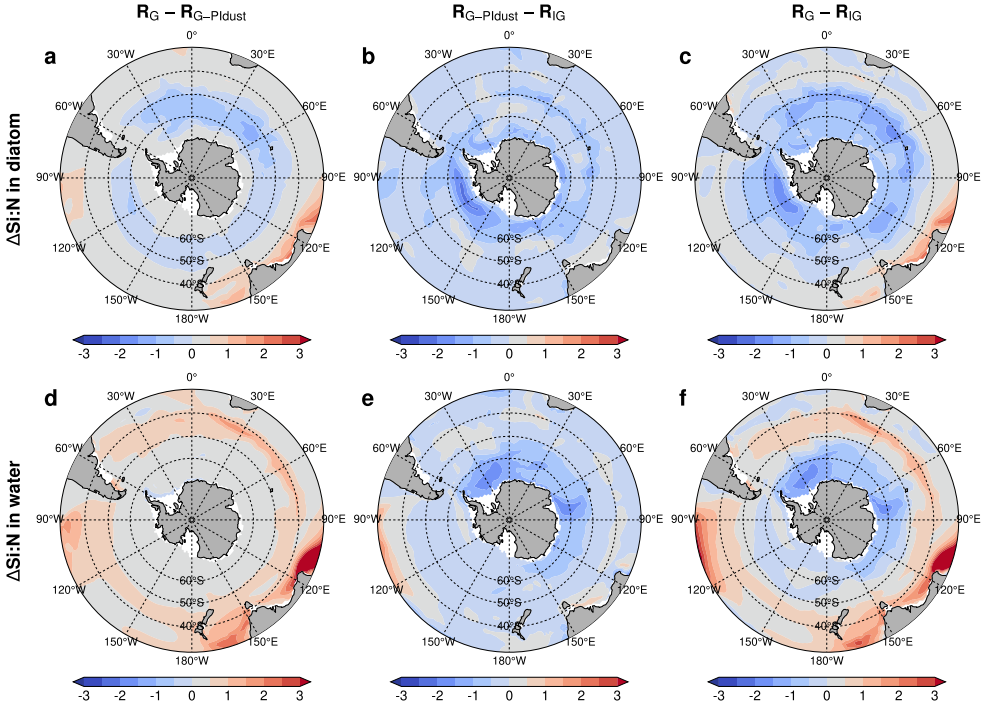


Figure 4. Si:N anomalies (mol Si mol N^{-1}) in diatoms (top) and surface seawater (bottom) south of 30° S: **(a, b)** effect of glacial dust (R_G–$R_{G\text{-}PIdust}$), **(c, d)** effect of the glacial climate ($R_{G\text{-}PIdust}$–R_{IG}) and **(e, f)** total glacial anomaly (R_G–R_{IG}).

3.4 Effect of glacial dust deposition on the Southern Ocean Si excess

To demonstrate the effect of enhanced glacial dust deposition on the SO Si excess, we compare R_{IG} and R_G with $R_{G\text{-}PIdust}$, in which PI dust deposition is applied under otherwise unchanged LGM conditions. The difference R_G–$R_{G\text{-}PIdust}$ shows the effect of glacial dust under glacial climate, and $R_{G\text{-}PIdust}$–R_{IG} the effect of the glacial climate (cooling, sea-ice expansion and associated circulation changes) under PI dust. Because the two effects may interact non-linearly, they do not necessarily add up to the total glacial anomaly (R_G–R_{IG}). Replacing LGM by PI dust raises atmospheric CO_2 by 12 ppm after 300 years, although the deep ocean has not fully adjusted within this period.

The two effects dominate in different regions of the SO (Fig. 4). The glacial climate lowers the Si:N ratio of diatom uptake mainly south of the APF, by up to about 2 mol Si mol N^{-1} (Fig. 4c), reflecting weaker nutrient stress when growth becomes increasingly light-limited under the expanded glacial sea ice, so that diatoms take up Si and N in a more coupled way. The glacial climate also lowers seawater Si:N throughout the SO surface by about 0.5 mol Si mol N^{-1} (up to 1.5 mol Si mol N^{-1} near the Antarctic margin; Fig. 4d). Since lower diatom Si:N alone would increase seawater Si:N, this decrease rather points to a physical cause, namely a reduced supply of Si-rich deep water under the expanded sea ice and stronger stratification. Glacial dust, in contrast, lowers the Si:N uptake ratio of diatoms mainly north of the APF, by up to about 1 mol Si mol N^{-1} (Fig. 4a),

https://doi.org/10.5194/egusphere-2026-6527
Preprint. Discussion started: 4 November 2026
© Author(s) 2026. CC BY 4.0 License.

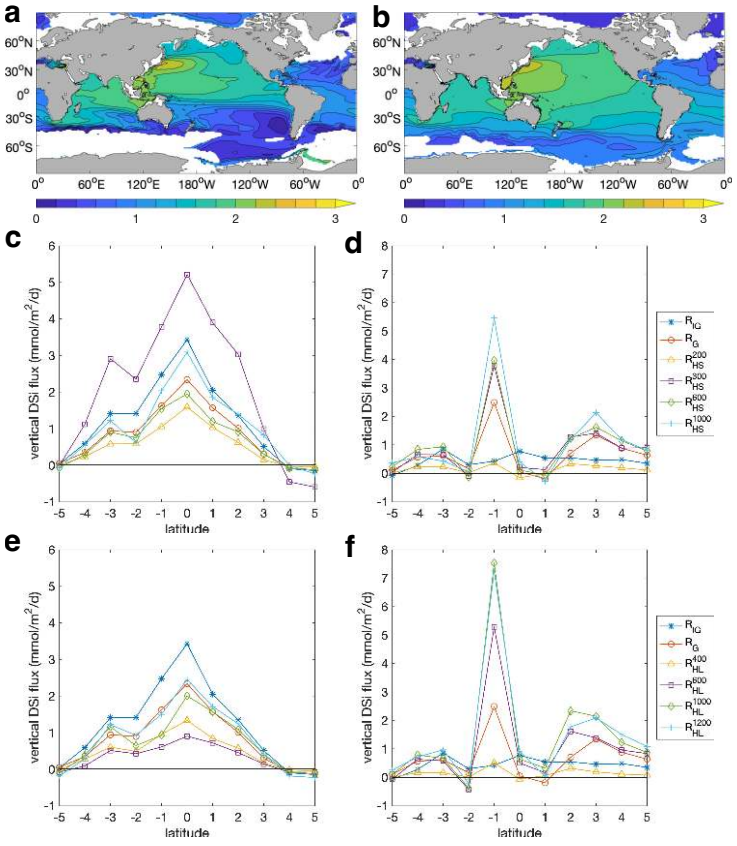


Figure 5. Si:N ratio (mmol Si mmol N^{-1}) along the typical isopycnal of Antarctic Intermediate Water (AAIW) (27.3 kg m^{-3} for PI and 27.8 kg m^{-3} for the LGM) in (a) R_{IG} and (b) R_G. Zonally averaged net upwelling flux of DSi (mmol Si m^{-2} d^{-1}) across 100 m depth in the tropical Pacific (c, e) and tropical Atlantic (d, f) in R_{HS} (c, d) and R_{HL} (e, f), together with R_{IG} and R_G.

where diatom NPP increases by 0.78 PgC yr^{-1} (+28 %). As a result, seawater Si:N rises by about 0.5–1 mol Si mol N^{-1} in the AAIW formation zone between 40 and 50° S (Fig. 4b) and by about 0.2–0.6 mol Si mol N^{-1} in intermediate waters. The increase follows the pathway of intermediate waters towards the low latitudes, but does not propagate into the low-latitude surface ocean, where changes in Si:N are minor (Fig. 6).

Taken together, enhanced dust deposition, rather than the glacial climate, is the main driver of the elevated Si:N ratios in SO surface waters and in the intermediate waters formed there in R_G, consistent with the premise of the SALH. Yet the dust-driven Si excess does not reach low-latitude diatoms: tropical (5° S–5° N) diatom NPP is even slightly lower in R_G than in $R_{G\text{-}PIdust}$ (-0.11 PgC yr^{-1}, -4 %). This confirms that the glacial Si leakage signal is generated by dust fertilisation but is prevented from reaching low-latitude diatoms by the physical constraints described in Sect. 3.3.

https://doi.org/10.5194/egusphere-2026-6527
Preprint. Discussion started: 4 November 2026
© Author(s) 2026. CC BY 4.0 License.

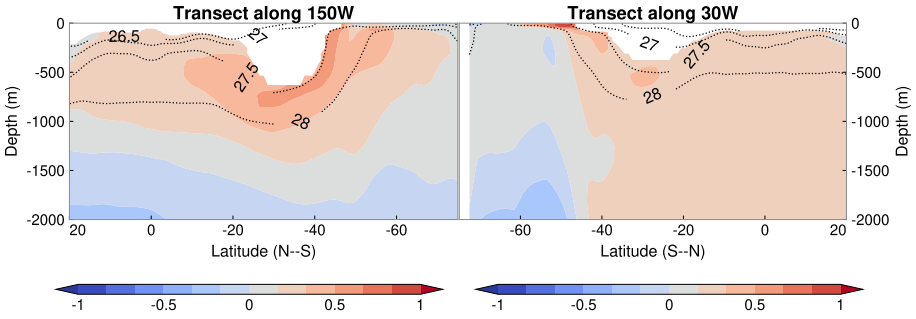


Figure 6. Difference in seawater Si:N ratio (DSi:DIN, mol mol^{-1}) between R_G and $R_{G\text{-PIdust}}$ (R_G–$R_{G\text{-PIdust}}$) along 150° W in the Pacific (left) and 30° W in the Atlantic (right) in the upper 2000 m. Positive values indicate higher Si:N under glacial dust deposition. Dotted black lines show potential density (σ_θ, kg m^{-3}) in $R_{G\text{-PIdust}}$. The ratio is calculated only where the dissolved inorganic nitrogen (DIN) concentration is at least 1 mmol m^{-3} in both simulations, because it becomes large and noisy in nutrient-depleted waters; these regions and the seafloor are masked in white.

3.5 Silicic acid redistribution in response to AMOC weakening and recovery

The freshwater perturbation in R_{HS} and R_{HL} produces several features that are also found in reconstructions of the early deglaciation, which started with HS1 about 18 kyr ago (Bard et al., 2000). First, freshwater input hampers the formation of North Atlantic Deep Water (NADW), reducing the AMOC from 19 Sv to about 5 Sv (Figs. 3d, h and A9), comparable to multi-proxy data–model estimates for HS1 (Pöppelmeier et al., 2023). Second, the AMOC weakening reduces the northward heat transport, causing NA cooling and SO warming via the bipolar seesaw (Fig. A10, R_{HS}^{200} and R_{HL}^{400}; Stocker and Johnsen, 2003). Third, the AMOC recovers rapidly after the freshwater input stops and stabilises at 22 Sv following an overshoot (Fig. 3d, h), in agreement with data (Barker et al., 2010) and other models (Pöppelmeier et al., 2023). As discussed in Sect. 2, these similarities concern the circulation response; the temporal evolution of the experiments should not be interpreted as a transient simulation of deglacial changes, since radiative forcing, ice sheets and dust deposition are held constant.

During the weak-AMOC phase (R_{HS}^{200} and R_{HL}^{400}), the pronounced AMOC weakening reduces nutrient supply from the deep ocean, particularly in the NA and the equatorial Pacific (Fig. 5c, e), lowering diatom growth and opal deposition onto sediments (Figs. 1c, d, f, g and 3e, i). The SO warming results in sea-ice retreat (Fig. A6), promoting SO ventilation and primary productivity in parts of the SO, also reflected in the opal deposition (Fig. 3e, i). Both stages exhibit higher DSi storage in the lower overturning cell compared to R_G (Figs. 7 and A11), driven by strong deep-ocean stratification, in agreement with δ^{30}Si and δ^{13}C records (Dumont et al., 2020). DSi concentrations in intermediate and mode waters are elevated compared to R_G; however, the slowdown of the overturning (Fig. A9b) and the deepening of these water masses (Fig. A7c) prevent this signal from substantially reaching low-latitude surface waters. Previous studies have also suggested that AMOC weakening is coherently linked to reduced northward penetration of AAIW in the Atlantic and to increased AAIW depth and thickness (e.g. Gu et al., 2017; Huang et al., 2014). This is corroborated by the simulated salinity along 30° W and the isopycnals along 30° W

https://doi.org/10.5194/egusphere-2026-6527
Preprint. Discussion started: 4 November 2026
© Author(s) 2026. CC BY 4.0 License.

and 150° W (Fig. A7c) and indicates little contribution of southern-sourced waters to the low-latitude nutrient supply during a weak AMOC. Globally, carbon export decreases by 14 %, with the strongest reduction in the NA, while diatom productivity decreases by 16 % (Fig. A4). A decline in the biological carbon pump alongside the AMOC weakening is consistent with $\delta^{13}C$ records for HS1 (Hertzberg et al., 2016) and may have been amplified by a concurrent reduction in aeolian iron supply. Under Marine Isotope Stage 3 conditions, changes in aeolian iron supply have been shown to add linearly to the AMOC-driven effect, resulting in a further atmospheric CO_2 rise of 6 ppm (Saini et al., 2024). The effect of aeolian iron input cannot be explored in our experiments, which prescribe a constant glacial aeolian iron supply.

In the recovered-AMOC phase (R_{HS}^{300}), the AMOC recovery promotes deep-water formation and northward heat transport, as well as increased formation of intermediate waters (Fig. A7d). Strengthened deep ventilation and transport of southern-sourced, Si-rich mode waters toward the low latitudes, together with enhanced wind-driven upwelling, mobilise nutrients from intermediate waters to the tropical surface ocean (Figs. 5c, d and 7). This signal is clearly reflected in the Si:N ratios of the equatorial Pacific and Atlantic surface waters (Fig. A8d). Global primary productivity returns to the level of R_G, with a strong increase in diatom growth and opal deposition in the tropics (Figs. 3f and A4). This opal peak, occurring after the reinvigoration of the overturning, is qualitatively similar to the opal accumulation recorded in many equatorial Atlantic and Pacific sediment cores during the BA (e.g. Bradtmiller et al., 2006, 2007) (Figs. 1 and A1), and supports the hypothesis that the reinvigoration of the overturning circulation during the deglaciation triggered a transient peak in nutrient supply to the low latitudes (Horn et al., 2011).

In R_{HL}^{600} and the following 200–300 years, the opal flux decreases clearly in the equatorial Pacific and increases slightly in the tropical Atlantic (Fig. 3j), despite a recovered and stabilised AMOC similar to R_{HS}^{300} (Fig. 3h). This is consistent with the lowest DSi supply to the tropical Pacific of the entire simulation and a higher DSi upwelling than at the LGM in the tropical Atlantic (Fig. 5e, f). The different behaviour of low-latitude nutrient supply and opal deposition between R_{HS} and R_{HL} during and after the AMOC resumption is attributed to the properties of the intermediate waters. In R_{HL}^{600}, the 28.5 kg m^{-3} isopycnal is substantially deepened, indicating a thicker layer of warmer intermediate waters resulting from the doubled freshwater input (Fig. A12). The expanded warm layer hinders exchange with nutrient-rich deeper waters, thereby weakening the upward supply of Si to low-latitude surface waters.

As biological productivity increases further, DSi becomes depleted in low-latitude surface waters (R_{HS}^{600} in Fig. 7), causing diatom growth to decline. A strong meridional overturning further mobilises deep-ocean nutrients, particularly from the deep Atlantic, into intermediate waters. This shifts the Si distribution from a pattern dominated by glacial deep storage to one characterised by enhanced surface supply (Fig. 5c–f) through intermediate waters (R_{HS}^{1000} in Fig. 7 and R_{HL}^{1200} in Fig. A11). The resulting opal peaks in R_{HS}^{1000} and R_{HL}^{1200} reflect this mobilisation of glacial deep-ocean Si, as suggested by the ASH for later deglacial stages (Dumont et al., 2020), rather than SO surface leakage.

3.6 Impact of surface Si leakage and deep Si mobilisation on the marine biological carbon pumps

During the first 100 years of both R_{HS} and R_{HL}, the SO exhibits enhanced CO_2 outgassing, concurrent with reduced high-latitude CO_2 uptake, driving a rapid CO_2 rise of 38 ppm (Fig. 3d, h). This increase is comparable to the ∼35 ppm rise found

https://doi.org/10.5194/egusphere-2026-6527
Preprint. Discussion started: 4 November 2026
© Author(s) 2026. CC BY 4.0 License.

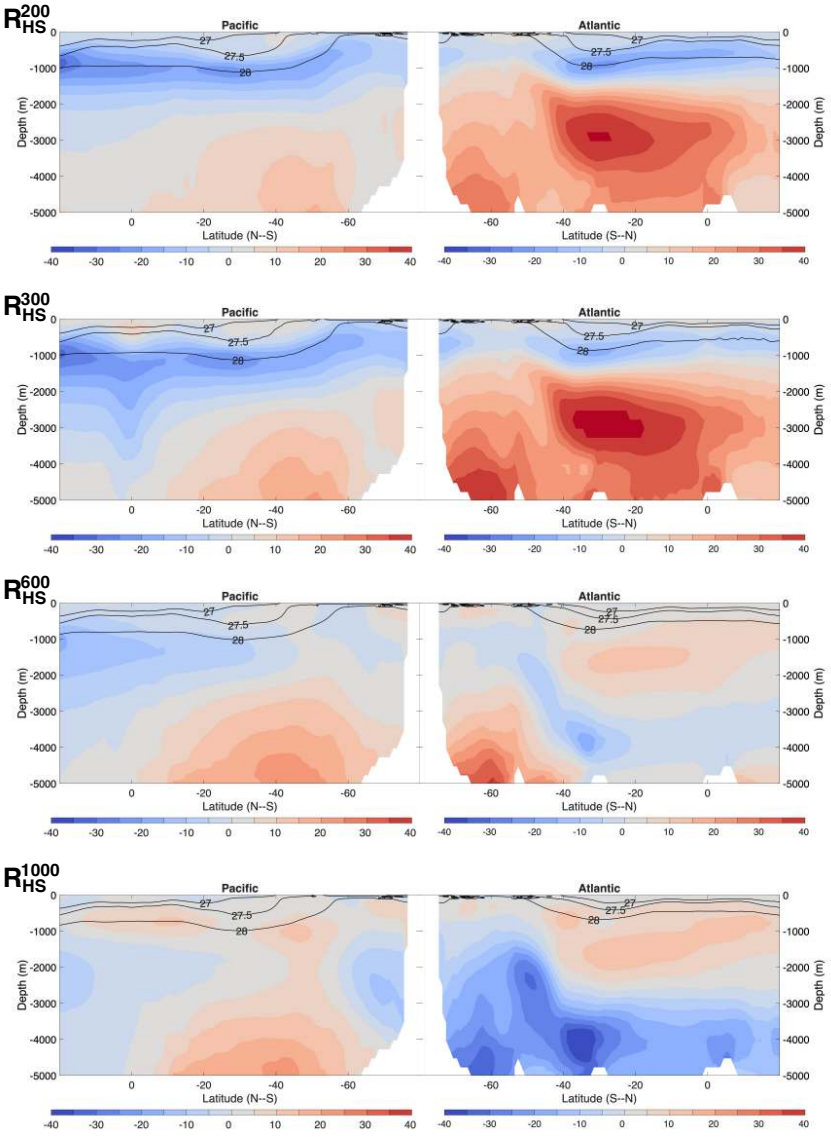


Figure 7. Anomaly (R_{HS}–R_G) of DSi (mmol Si m^{-3}) at model years 200, 300, 600 and 1000, zonally averaged for the Pacific (left) and Atlantic (right). Isopycnals (kg m^{-3}) around the intermediate waters are shown as black lines.

https://doi.org/10.5194/egusphere-2026-6527
Preprint. Discussion started: 4 November 2026
© Author(s) 2026. CC BY 4.0 License.

in ice cores for HS1 (Marcott et al., 2014), albeit over a much shorter period. Subsequently, the rate of increase declines substantially.

Reduced nutrient supply to the tropical surface ocean favours the growth of smaller phytoplankton, including calcifiers, which have higher surface-to-volume ratios than large diatoms. Consequently, $CaCO_3$:POC export ratios in the tropical ocean increase in both R_{HS} and R_{HL} compared to R_G (Fig. A4; from 0.073 to >0.1), indicating a substantial strengthening of the carbonate counter pump relative to the soft-tissue pump. Yet changes in CO_2 fluxes at low latitudes remain small (less than 5 % enhanced outgassing relative to R_G), whereas warming in the SO leads to enhanced outgassing that dominates the CO_2 rise.

After the freshwater inflow stops, the atmospheric CO_2 rise stagnates between years 250 and 350 in R_{HS} and for a shorter period of ∼70 years in R_{HL}. Si leakage from the SO surface induces a short but intensive diatom bloom, increasing tropical diatom productivity (5° S–5° N) by 30 % in R_{HS}^{300} compared to R_{HS}^{200} and reducing the tropical $CaCO_3$:POC export ratio from 0.11 to 0.09 (Fig. A4). The overall efficiency of the biological carbon pump thus becomes higher in the tropical ocean, coinciding with the stagnation of the CO_2 rise. The enhanced ocean CO_2 uptake in the tropical ocean (up to 15 %) remains, however, small relative to the enhancement in deep-water formation regions, which exceeds 100 % in some cases.

Following the stagnation phase, atmospheric CO_2 rises further and gradually in both simulations, with values in R_{HL} slightly higher than in R_{HS} (Fig. 3d, h). By the end of the two simulations, Si upwelling from the deep ocean triggers a less pronounced but more persistent diatom bloom in the tropical ocean and increases POC export by 32 % in R_{HS} and 45 % in R_{HL} relative to the weak-AMOC phase (Fig. A4). The tropical $CaCO_3$:POC export ratio drops further to 0.06. These changes in the biological carbon pumps likely contribute to stabilising atmospheric CO_2, although the progressive outgassing driven by warming and sea-ice retreat dominates the air–sea CO_2 flux until the end of the simulations (Figs. A6 and A10).

4 Discussion and conclusions: revising previous hypotheses

Our results show both agreement with and divergence to previous hypotheses on the glacial and deglacial Si cycle. Consistent with the SALH, the LGM simulation exhibits reduced Si:N ratios in uptake by diatoms in the SO, driven by enhanced glacial aeolian iron input, resulting in elevated Si:N ratios in AAIW. The sensitivity experiment with PI dust deposition ($R_{G\text{-}PIdust}$) demonstrates that this Si excess in SO surface and intermediate waters is driven by glacial dust deposition, whereas the glacial climate alone lowers surface-water Si:N in the SO. We found elevated DSi concentrations in AAIW already during the LGM (Fig. 8, LGM), rather than a first increase during HS1 as suggested by the SAVH. Strong stratification, weakened AAIW formation and low-latitude upwelling at the LGM, however, prevent efficient transport of the Si-enriched intermediate water to the tropical surface ocean, limiting diatom growth and its potential contribution to glacial CO_2 drawdown, in disagreement with the SALH. The same applies to the corollary of Matsumoto and Sarmiento (2008): since the waters reaching the tropical surface ocean are not enriched in Si relative to N, the simulated tropical export shifts slightly towards calcifiers rather than diatoms. Although our simulation may overestimate the Si source in SO surface waters forming the glacial AAIW, the absence of a pronounced opal enhancement in the equatorial ocean further supports that Si leakage was not successfully transported to low latitudes during the LGM.

https://doi.org/10.5194/egusphere-2026-6527
Preprint. Discussion started: 4 November 2026
© Author(s) 2026. CC BY 4.0 License.

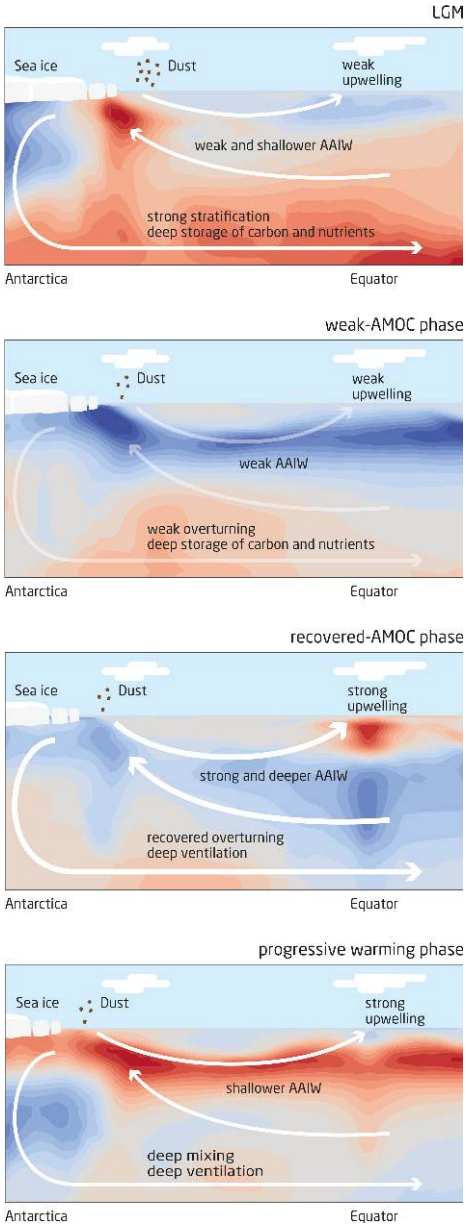


Figure 8. Conceptual schematic of changes in the marine silicon cycle in the Southern Hemisphere across the deglaciation, derived from the simulations. White lines depict the major overturning circulation; semi-transparent lines indicate a weakened, slower overturning. Brown dots above the ocean surface represent aeolian dust deposition. Background shading illustrates simulated changes in DSi concentrations. "LGM": DSi anomalies of the LGM relative to the PI simulation; "weak-AMOC phase": DSi anomalies in R_{HS} during the AMOC slowdown relative to the LGM simulation; "recovered-AMOC phase": DSi anomalies in R_{HS} following AMOC recovery relative to the weak-AMOC phase; "progressive-warming phase": DSi anomalies at the end of R_{HS}, characterised by continued sea-ice retreat and strengthened SO ventilation, relative to the LGM simulation.

https://doi.org/10.5194/egusphere-2026-6527
Preprint. Discussion started: 4 November 2026
© Author(s) 2026. CC BY 4.0 License.

Our hosing experiments demonstrate deglacial scenarios in which low-latitude productivity is primarily controlled by changes in circulation and associated nutrient supply. During the weak-AMOC phase (Fig. 8), deep-ocean ventilation and exchange between deep and intermediate waters were substantially reduced. Although SO surface warming and sea-ice retreat may have enhanced local overturning and upwelling, the global deep-ocean Si storage increased further, while DSi concentrations in intermediate waters decreased relative to the LGM level. The equatorward transport of Si leaked from the SO surface ocean was strongly constrained by reduced high-latitude formation of intermediate waters. Limited low-latitude upwelling restricted exchange with underlying waters, preventing a substantial increase in Si supply to the tropical surface ocean. As a result, diatom productivity remained unchanged or declined. Some opal records across the tropical ocean document higher accumulation rates during HS1 relative to the LGM (Fig. A1), implying that the freshwater perturbation experiments may not capture all climatic influences on low-latitude productivity during HS1 and should be best viewed as a mechanistic exploration of how deglacial circulation changes could affect low-latitude nutrient supply, rather than as a direct simulation of HS1 conditions. Importantly, the simulated opal peak associated with the reinvigoration of overturning is consistent with reconstructions, supporting the robustness of the identified timing of enhanced Si supply following AMOC recovery. Prescribing LGM dust deposition throughout the hosing experiments, however, may lead to an overestimation of the magnitude of Si leakage.

Resumption of the meridional overturning (Fig. 8, recovered-AMOC phase) strengthened intermediate water formation, promoted Si supply from the SO surface leakage and initialised the mobilisation of the deep Si storage. In our hosing experiments, freshwater addition was terminated abruptly and the redistribution of Si from the deep ocean to intermediate waters occurred several hundred model years later (Fig. 8, progressive-warming phase). The freshwater input from iceberg discharge during the last deglaciation persisted over millennia, likely allowing a gradual transition from surface leakage to deep mobilisation of Si, which could explain why opal peaks have been observed across different records over a longer time period following HS1. Testing this hypothesis, however, requires fully transient deglacial simulations rather than idealised hosing experiments.

Taken together, this study reveals the two distinct mechanisms supplying Si to low-latitude surface waters during the deglaciation and links opal peaks in sediment records to freshwater events: (1) reinvigoration of overturning transports and upwells Si that leaked from the SO surface waters, producing short-lived but pronounced peaks of diatom growth and opal export in the tropical ocean; and (2) continued warming and sea-ice retreat later in the deglaciation mobilise the large glacial Si reservoir in the deep ocean, sustaining more persistent enhancement of diatom growth globally. Although the set-up of our hosing experiments is too idealised for direct comparison with deglacial stages, the first mechanism is analogous to the SAVH but operates after AMOC recovery, while the second aligns with processes proposed by the ASH. Despite some discrepancies in timing, our concept reconciles previous hypotheses within a unified framework, defining circulation recovery as the critical trigger that links freshwater forcing to sedimentary opal records. Attributing individual deglacial opal peaks in sediment records to different mechanisms identified in this study remains challenging, encouraging future studies to integrate high-temporal-resolution reconstructions of freshwater inputs, deep-water influences and opal accumulation throughout the deglaciation.

Our hosing experiments, accounting for varying amounts of freshwater input, demonstrate that a short but intense freshwater pulse in the North Atlantic stimulates the upwelling of leaked Si accumulated in intermediate waters, whereas a prolonged

https://doi.org/10.5194/egusphere-2026-6527
Preprint. Discussion started: 4 November 2026
© Author(s) 2026. CC BY 4.0 License.



melting event delivering larger freshwater volumes primarily alters the volume and stratification of intermediate waters, thereby suppressing the upwelling of leaked Si to the low-latitude surface ocean. Together, these results provide new insights into how the marine carbon pump may respond to future climate scenarios involving meltwater inputs of varying duration and intensity.

Code availability. The source code of FESOM2.1-REcoM3p is archived on Zenodo (Ye, 2023). The atmosphere model ECHAM6 is property of the Max Planck Institute for Meteorology.

Data availability. Model output required to reproduce the figures will be made available on Zenodo upon publication and is accessible to the reviewers during the review process. The compiled opal accumulation rates are provided in Tables S1 (Atlantic) and S2 (Pacific) in the Supplement and will also be made available on Zenodo upon publication. All reconstructions used are from published studies cited in Sect. 2.4.

https://doi.org/10.5194/egusphere-2026-6527
Preprint. Discussion started: 4 November 2026
© Author(s) 2026. CC BY 4.0 License.

Appendix A: Additional figures

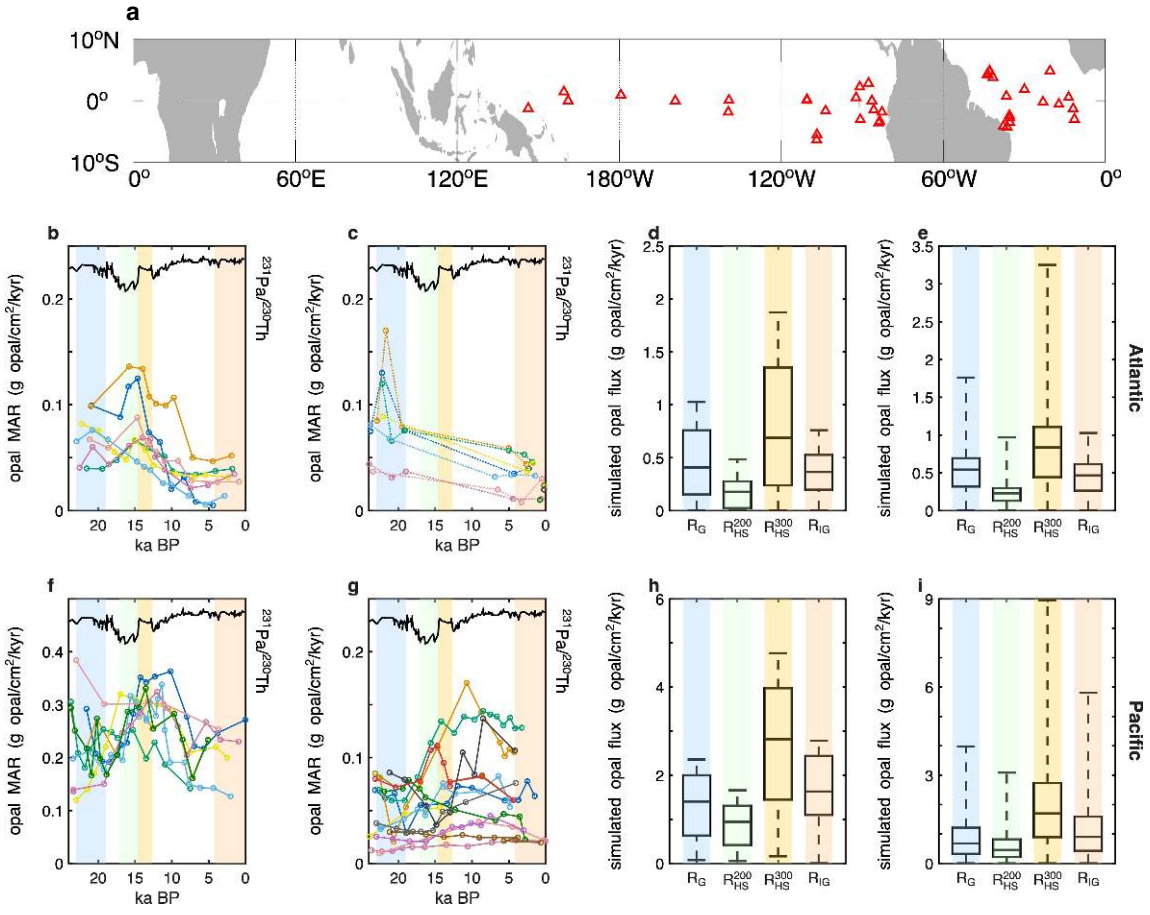


Figure A1. Reconstructed marine opal accumulation rates from 24 kyr BP to present (Bradtmiller et al., 2006, 2007; Kienast et al., 2006; Richaud et al., 2007; Pichevin et al., 2009; Dubois et al., 2010; Lippold et al., 2012), compared with simulated opal fluxes to the seafloor. **(a)** Locations of cores used for panels (b), (c), (f) and (g). **(b, c)** Equatorial Atlantic reconstructions grouped into cores showing deglacial trends (b) and those covering only the Holocene and LGM (c). **(f, g)** Equatorial Pacific reconstructions grouped into high-accumulation (f) and low-accumulation cores (g), depending on whether the maximum opal MAR between 0 and 24 ka exceeds 0.25 g opal cm^{-2} kyr^{-1}, an operational criterion to make temporal trends in the low-accumulation cores visible. Individual core records are shown as coloured lines. Coloured background bars indicate the LGM (23–19 ka, light blue), HS1 (17.07–14.59 ka, light green), BA (14.59–12.68 ka, light yellow) and late Holocene (4.2–0 ka, light orange); the HS1 and BA periods are derived from the $^{231}Pa/^{230}Th$ record at Bermuda Rise and its age model (Lippold et al., 2019) (black line, inverted axis with stronger AMOC upward). **(d, h)** Simulated opal flux to sediments at the core locations in the equatorial Atlantic (d) and Pacific (h) for R_G, R_{HS}^{200}, R_{HS}^{300} and R_{IG}, shown as box plots on coloured stripes reflecting the analogous AMOC states. Boxes show the 0.25–0.75 quantiles, whiskers the full range, and horizontal lines the medians. **(e, i)** As (d) and (h) but averaged over the tropical Atlantic and Pacific (5° S–5° N).

https://doi.org/10.5194/egusphere-2026-6527
Preprint. Discussion started: 4 November 2026
© Author(s) 2026. CC BY 4.0 License.

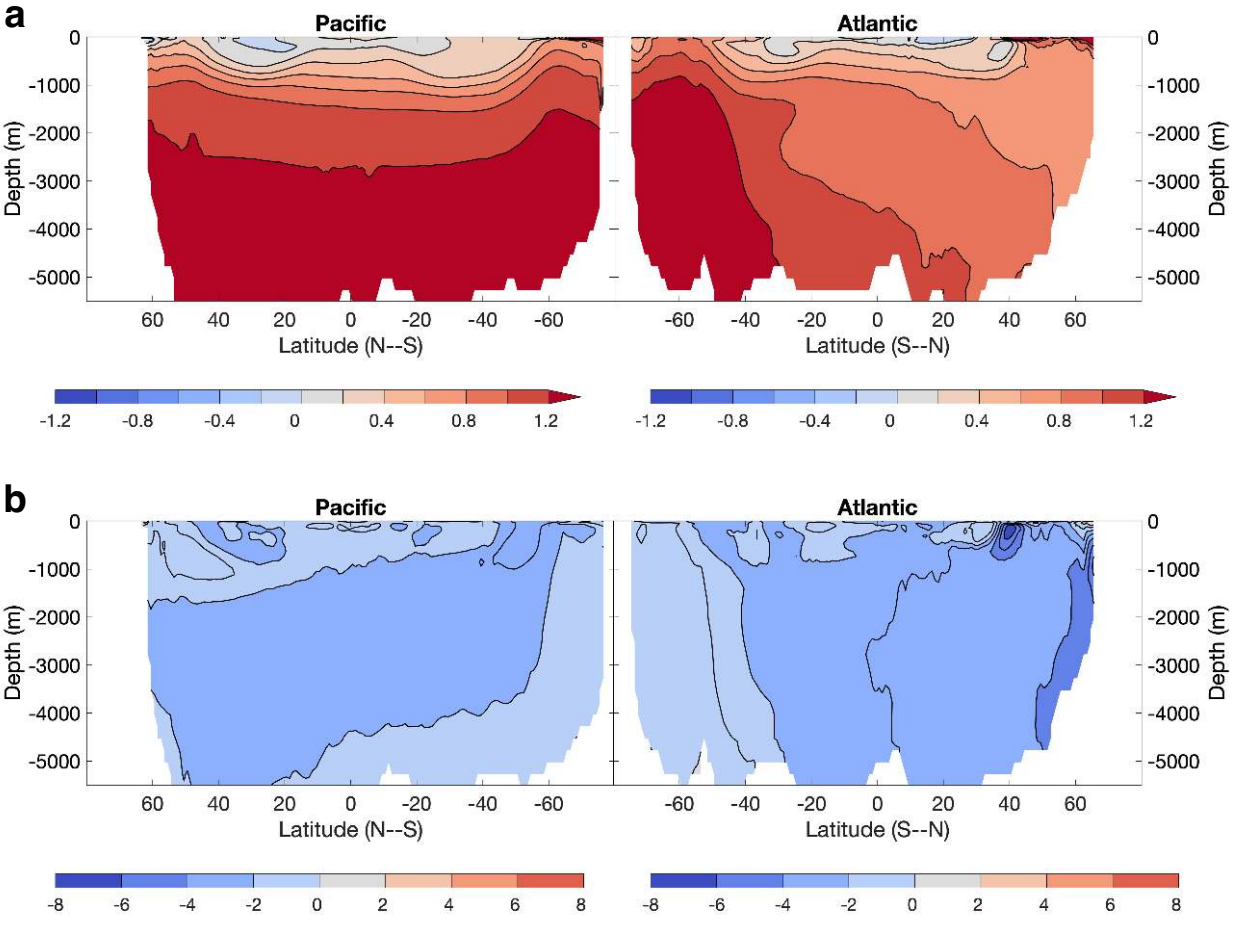


Figure A2. Anomaly (R_G–R_{IG}) of (a) salinity and (b) temperature (°C), zonally averaged for the Pacific and Atlantic.

https://doi.org/10.5194/egusphere-2026-6527
Preprint. Discussion started: 4 November 2026
© Author(s) 2026. CC BY 4.0 License.

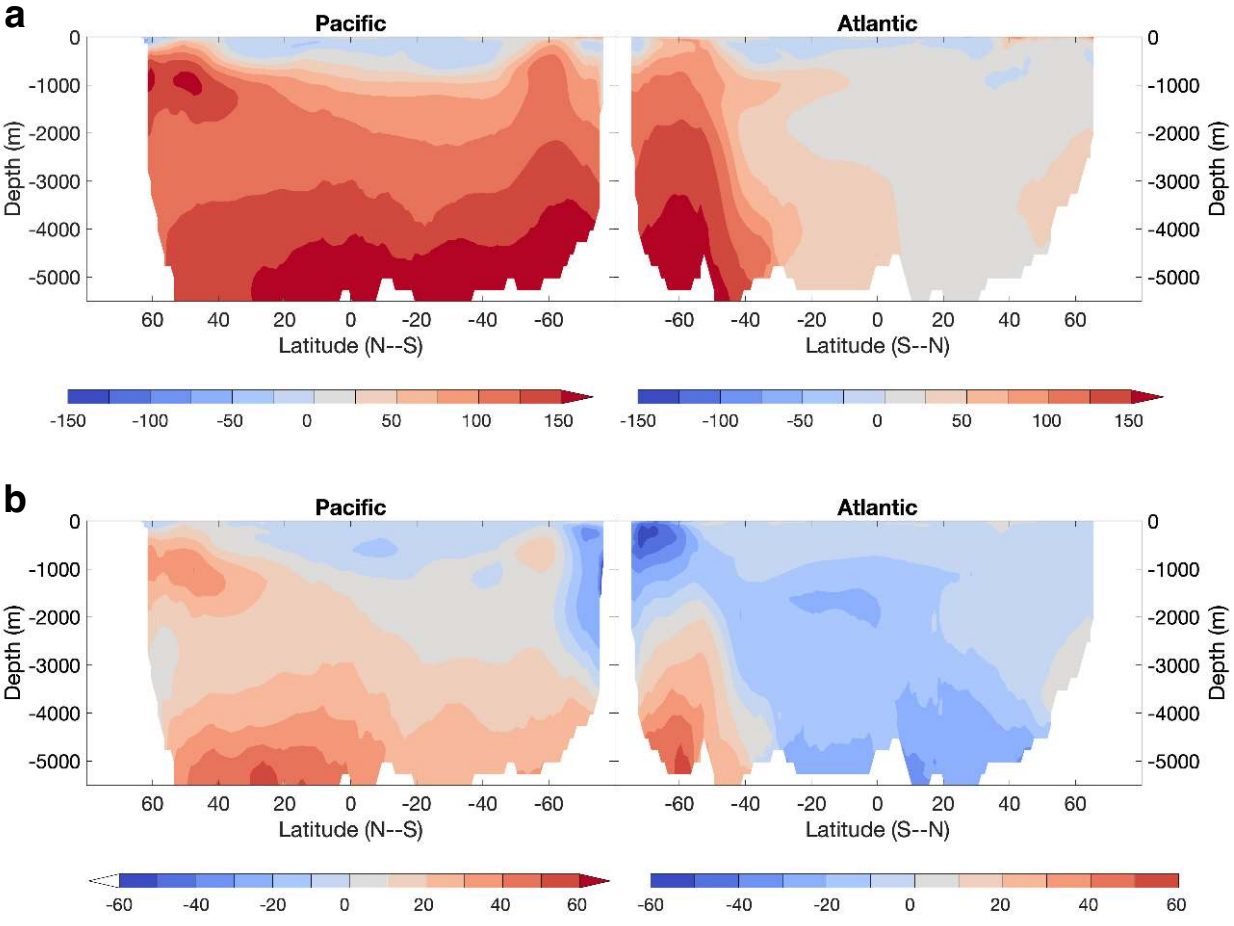


Figure A3. Anomaly (R_G–R_{IG}) of (a) DIC (mmol C m^{-3}) and (b) DSi (mmol Si m^{-3}), zonally averaged for the Pacific and Atlantic.

https://doi.org/10.5194/egusphere-2026-6527
Preprint. Discussion started: 4 November 2026
© Author(s) 2026. CC BY 4.0 License.

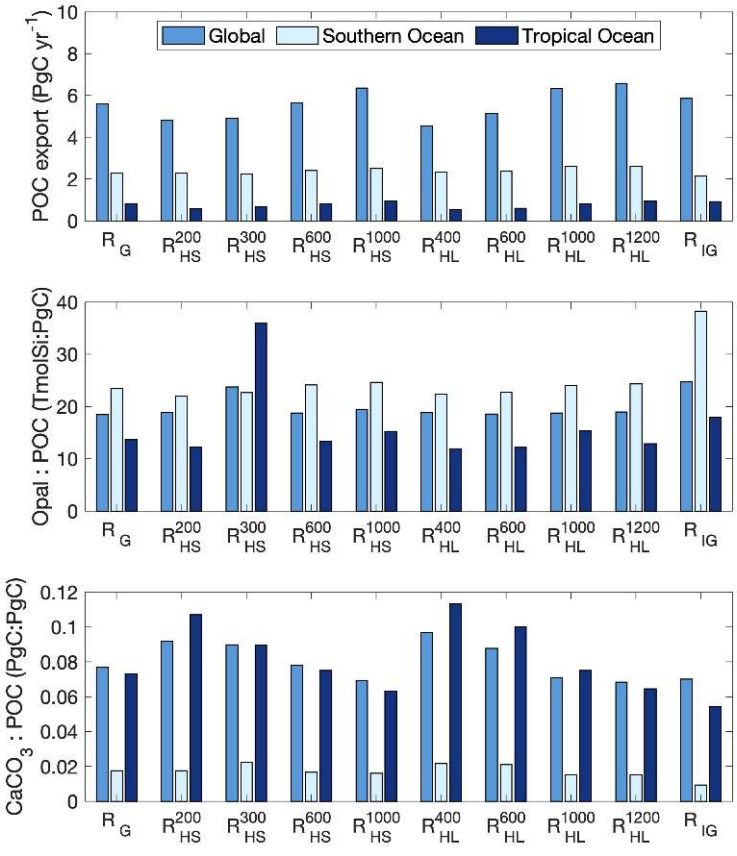


Figure A4. Simulated export fluxes of particulate organic carbon (POC; PgC yr^{-1}), opal:POC ratios (Tmol Si PgC^{-1}) and $CaCO_3$:POC ratios (PgC PgC^{-1}) at 100 m depth for the global ocean, the Southern Ocean (south of 40° S) and the tropical ocean (5° S–5° N) in R_G, at each key stage of R_{HS} and R_{HL}, and in R_{IG}.

https://doi.org/10.5194/egusphere-2026-6527
Preprint. Discussion started: 4 November 2026
© Author(s) 2026. CC BY 4.0 License.

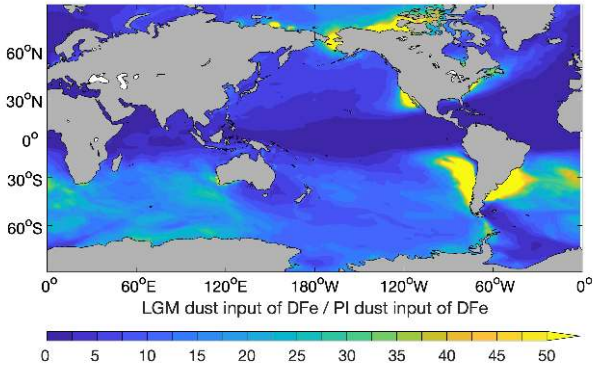


Figure A5. Enhancement of the dust input of dissolved iron during the LGM (R_G/R_{IG}) according to the prescribed dust deposition fluxes (Albani et al., 2014). Globally, the dust source of iron increases from 6 to 10 Gmol Fe yr^{-1}, the largest glacial–interglacial change in external iron sources in our simulations; the riverine source rises from 5.2 to 6 Gmol Fe yr^{-1} due to increased runoff, and the sedimentary source declines from 2.6 to 1.6 Gmol Fe yr^{-1} as a result of sea-level lowering.

https://doi.org/10.5194/egusphere-2026-6527
Preprint. Discussion started: 4 November 2026
© Author(s) 2026. CC BY 4.0 License.

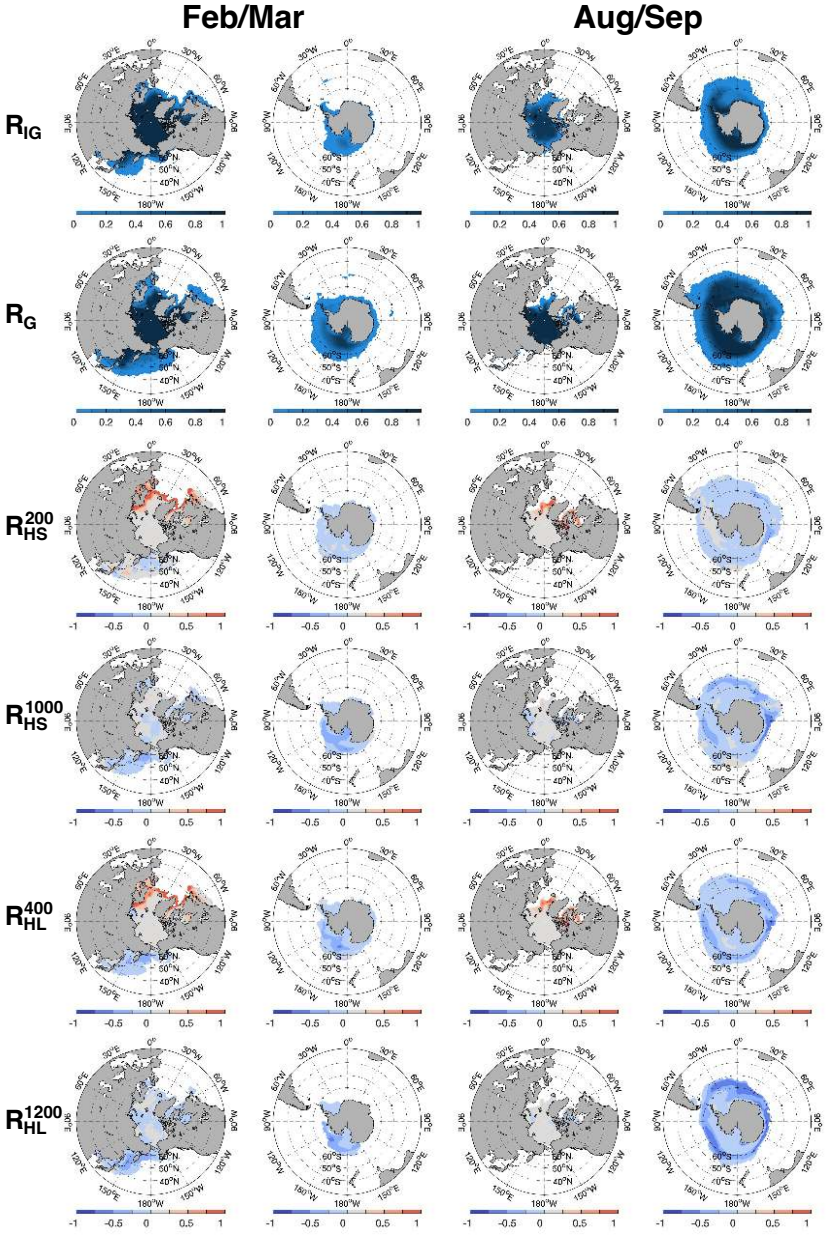


Figure A6. Sea-ice concentration in R_G and its anomaly in R_{HS} and R_{HL} relative to R_G, averaged over February and March (maximum extent in the Northern Hemisphere) and over August and September (maximum extent in the Southern Hemisphere), for the weak-AMOC phase and the final state of the experiments.

https://doi.org/10.5194/egusphere-2026-6527
Preprint. Discussion started: 4 November 2026
© Author(s) 2026. CC BY 4.0 License.

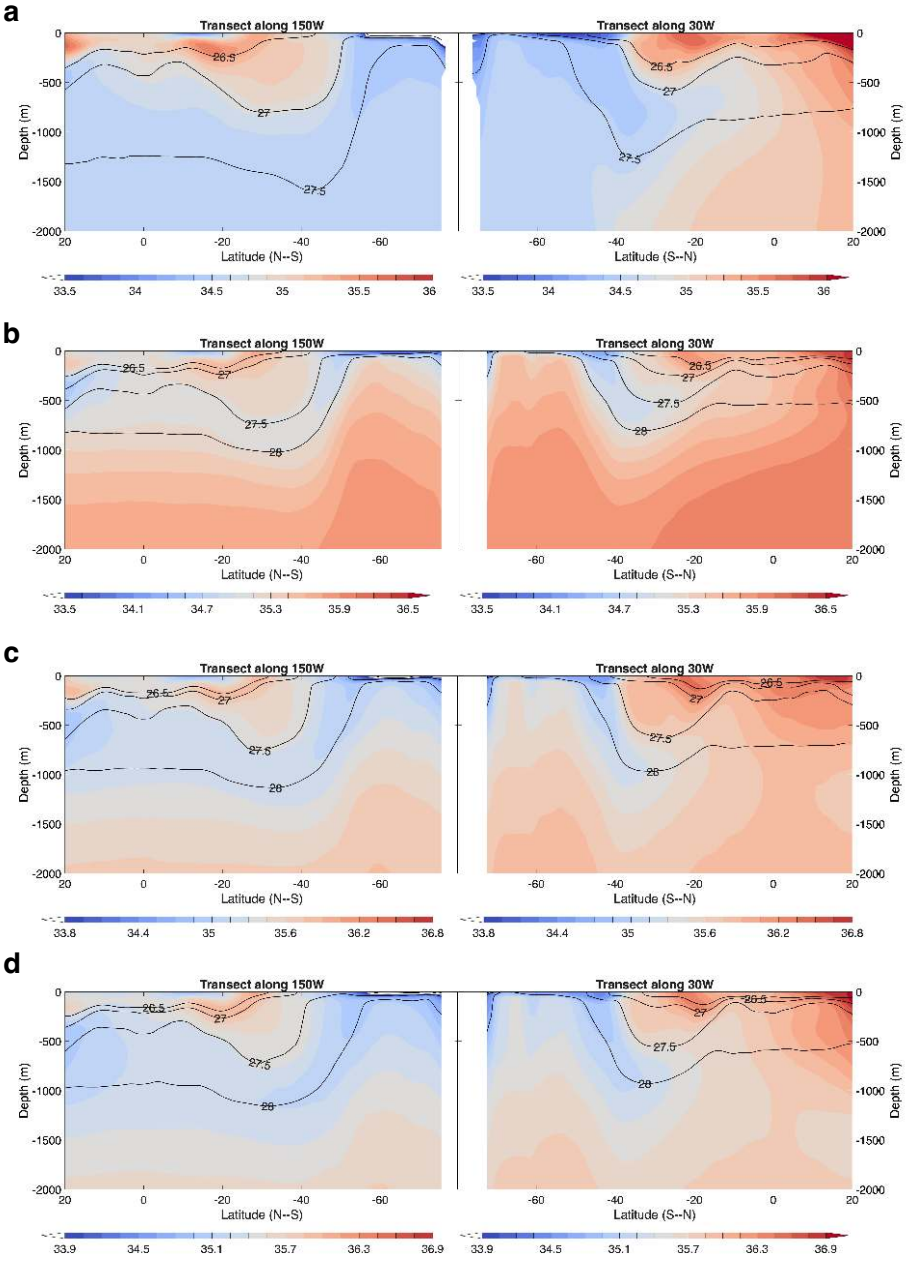


Figure A7. Salinity along transects at 30° W and 150° W, overlaid by σ_θ from 26.5 to 28 kg m^{-3}, for (a) R_{IG}, (b) R_G, (c) R_{HS}^{200} and (d) R_{HS}^{300}.

https://doi.org/10.5194/egusphere-2026-6527
Preprint. Discussion started: 4 November 2026
© Author(s) 2026. CC BY 4.0 License.

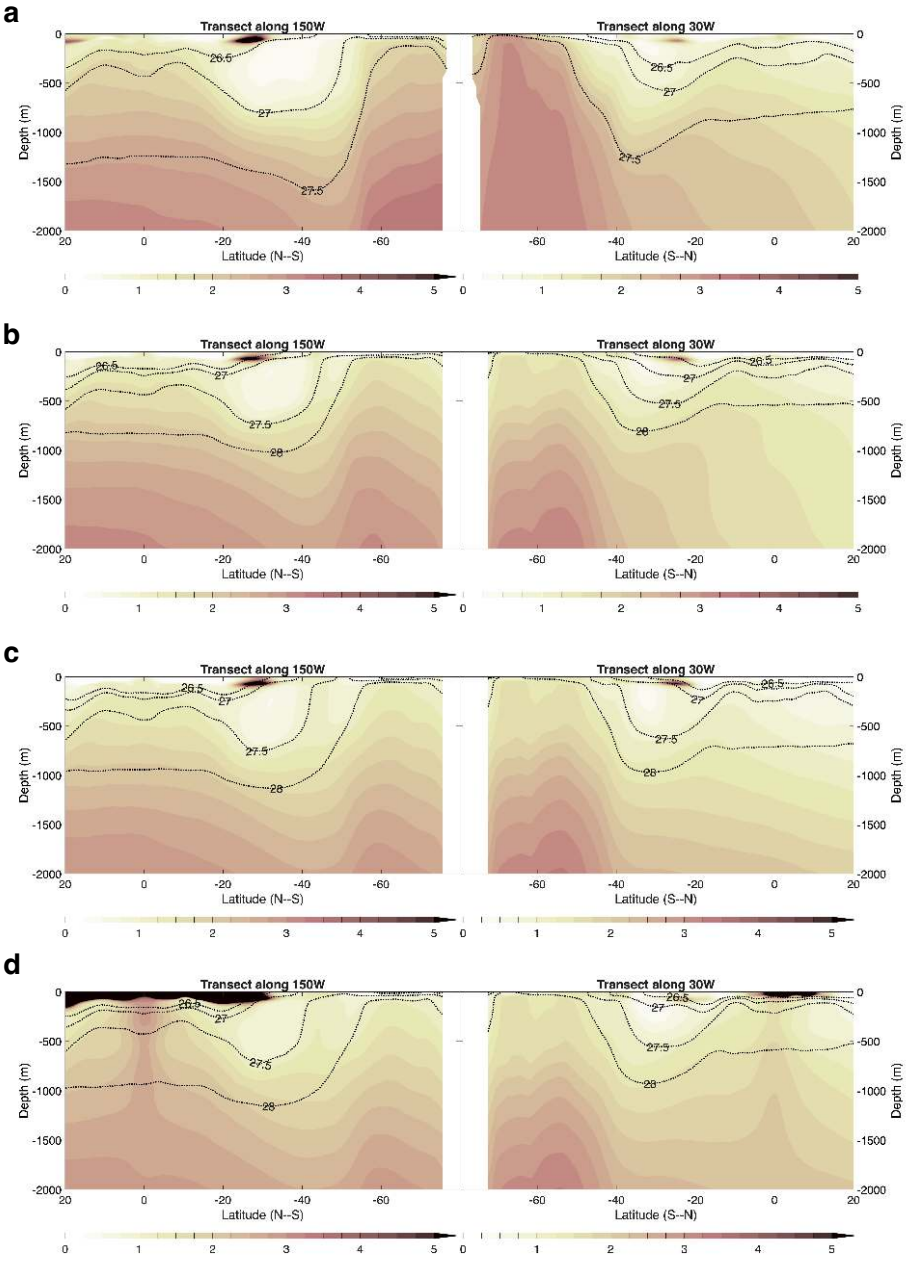


Figure A8. Si:N ratios (mmol Si mmol N^{-1}) along transects at 30° W and 150° W, overlaid by σ_θ from 26.5 to 28 kg m^{-3}, for (a) R_{IG}, (b) R_G, (c) R_{HS}^{200} and (d) R_{HS}^{300}.

https://doi.org/10.5194/egusphere-2026-6527
Preprint. Discussion started: 4 November 2026
© Author(s) 2026. CC BY 4.0 License.

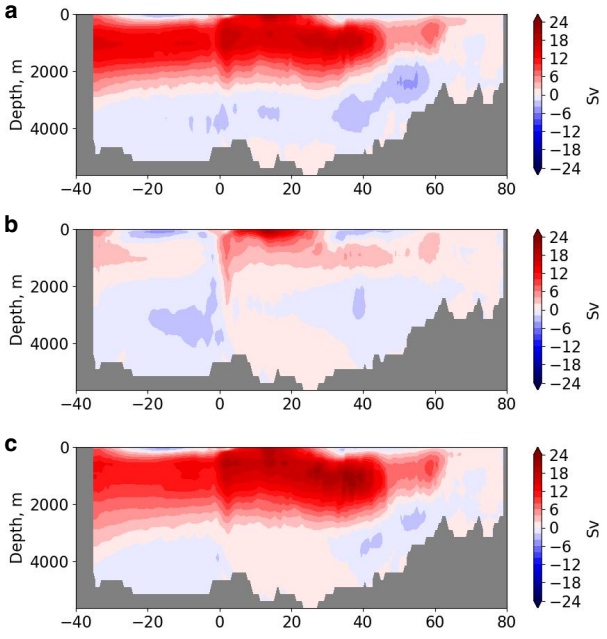


Figure A9. Atlantic Meridional Overturning Circulation (Sv) in (a) R_G and in R_{HS} at (b) year 200 and (c) year 300. The weakened and recovered AMOC in R_{HL} shows a similar pattern.

https://doi.org/10.5194/egusphere-2026-6527
Preprint. Discussion started: 4 November 2026
© Author(s) 2026. CC BY 4.0 License.

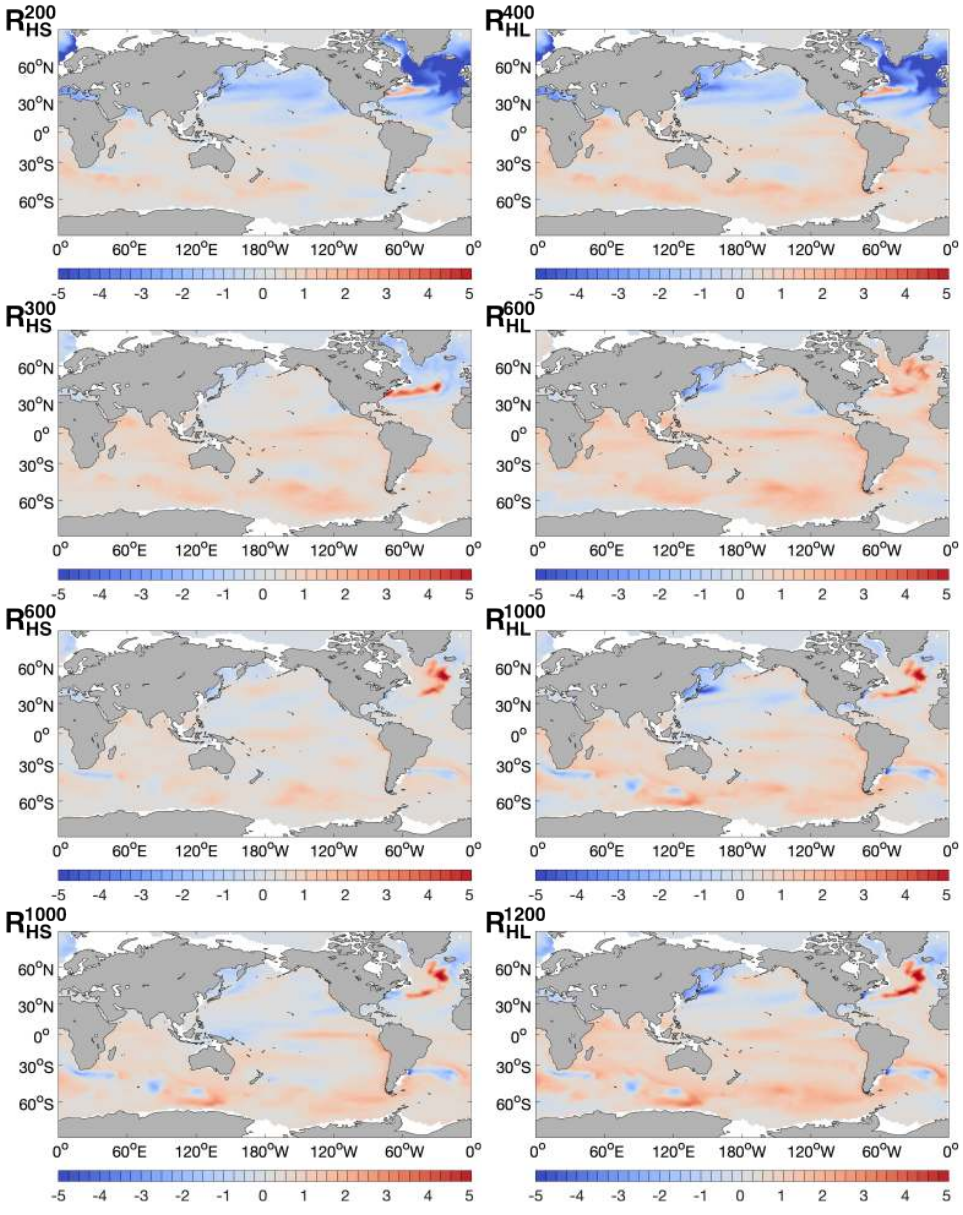


Figure A10. Changes in SST (°C) in R_{HS} (years 200, 300, 600 and 1000) and R_{HL} (years 400, 600, 1000 and 1200) relative to R_G.

https://doi.org/10.5194/egusphere-2026-6527
Preprint. Discussion started: 4 November 2026
© Author(s) 2026. CC BY 4.0 License.

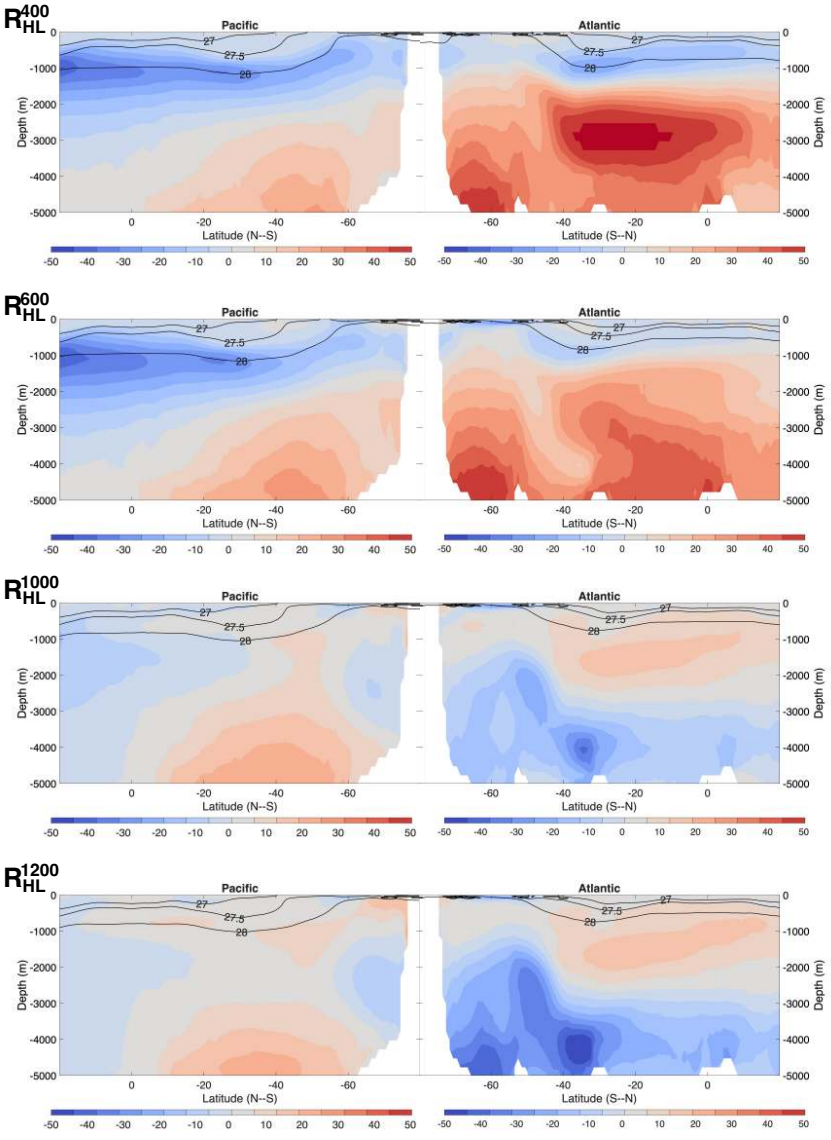


Figure A11. Anomaly (R_{HL}–R_G) of DSi (mmol Si m^{-3}) at model years 400, 600, 1000 and 1200, zonally averaged for the Pacific and Atlantic. Isopycnals (kg m^{-3}) around the intermediate waters are shown as black lines.

https://doi.org/10.5194/egusphere-2026-6527
Preprint. Discussion started: 4 November 2026
© Author(s) 2026. CC BY 4.0 License.

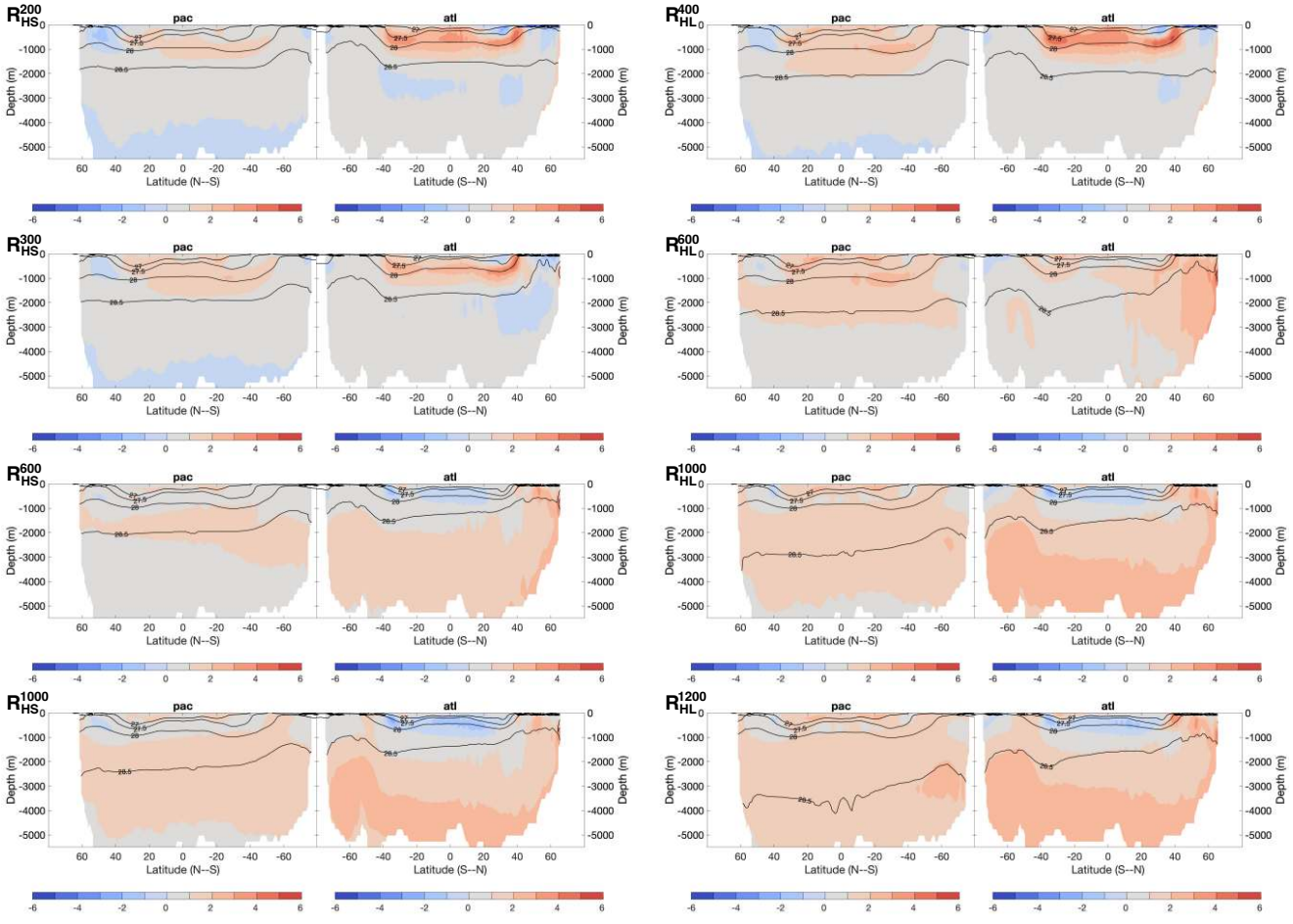


Figure A12. Changes in temperature (°C) in R_{HS} (years 200, 300, 600 and 1000; left) and R_{HL} (years 400, 600, 1000 and 1200; right) relative to R_G, zonally averaged for the Pacific and Atlantic. Isopycnals around the intermediate waters are shown as black lines.

https://doi.org/10.5194/egusphere-2026-6527
Preprint. Discussion started: 4 November 2026
© Author(s) 2026. CC BY 4.0 License.

Author contributions. Conceptualisation: YY, PK, CV. Project administration: PK, CV. Software: YY, MB. YY performed the simulations and analysed and visualised the results. All authors contributed to writing the paper and to the discussion of the results.

Competing interests. The authors declare that they have no conflict of interest.

Acknowledgements. We thank Qiyun Ma, Yuchen Sun, Walter Geibert, Patrick Scholz and Dmitry Sidorenko for discussions, Yves Nowak for graphic support with Fig. 8, and Nathalie Dubois, Mathieu Richaud and Christopher Hayes for providing opal data. Simulations were performed at the German Climate Computing Center (DKRZ), project ID: BM1030. An AI assistant (Claude, Anthropic) was used to help edit the text; all content was checked by the authors.

Financial support. This research has been supported by the German Federal Ministry of Education and Research (BMBF) through the German Climate Modelling Initiative PalMod, phases II and III (grant nos. 01LP1919A and 01LP2319A).

https://doi.org/10.5194/egusphere-2026-6527
Preprint. Discussion started: 4 November 2026
© Author(s) 2026. CC BY 4.0 License.

References

Ackermann, L., Rackow, T., Himstedt, K., Gierz, P., Knorr, G., and Lohmann, G.: A comprehensive Earth system model (AWI-ESM2.1) with interactive icebergs: effects on surface and deep-ocean characteristics, Geoscientific Model Development, 17, 3279–3301, https://doi.org/10.5194/gmd-17-3279-2024, 2024.

Albani, S., Mahowald, N. M., Perry, A. T., Scanza, R. A., Zender, C. S., Heavens, N. G., Maggi, V., Kok, J. F., and Otto-Bliesner, B. L.: Improved Dust Representation in the Community Atmosphere Model, Journal of Advances in Modeling Earth Systems, 6, 541–570, https://doi.org/10.1002/2013MS000279, 2014.

Aumont, O., Ethé, C., Tagliabue, A., Bopp, L., and Gehlen, M.: PISCES-v2: An Ocean Biogeochemical Model for Carbon and Ecosystem Studies, Geoscientific Model Development, 8, 2465–2513, https://doi.org/10.5194/gmd-8-2465-2015, 2015.

Bard, E., Rostek, F., Turon, J.-L., and Gendreau, S.: Hydrological impact of Heinrich events in the subtropical northeast Atlantic, Science, 289, 1321–1324, https://doi.org/10.1126/science.289.5483.132, 2000.

Barker, S., Knorr, G., Vautravers, M. J., Diz, P., and Skinner, L. C.: Extreme deepening of the Atlantic overturning circulation during deglaciation, Nature Geoscience, 3, 567–571, https://doi.org/10.1038/ngeo921, 2010.

Bereiter, B., Eggleston, S., Schmitt, J., Nehrbass-Ahles, C., Stocker, T. F., Fischer, H., Kipfstuhl, S., and Chappellaz, J.: Revision of the EPICA Dome C CO_2 record from 800 to 600 kyr before present, Geophysical Research Letters, 42, 542–549, https://doi.org/10.1002/2014GL061957, 2015.

Berger, A. and Loutre, M.: Insolation values for the climate of the last 10 million years, Quaternary Science Reviews, 10, 297–317, https://doi.org/https://doi.org/10.1016/0277-3791(91)90033-Q, 1991.

Beucher, C. P., Brzezinski, M. A., and Crosta, X.: Silicic acid dynamics in the glacial sub-Antarctic: Implications for the silicic acid leakage hypothesis, Global Biogeochemical Cycles, 21, GB3015, https://doi.org/10.1029/2006GB002746, 2007.

Bostock, H. C., Opdyke, B. N., Gagan, M. K., and Fifield, L. K.: Carbon isotope evidence for changes in Antarctic Intermediate Water circulation and ocean ventilation in the southwest Pacific during the last deglaciation, Paleoceanography, 19, PA4013, https://doi.org/10.1029/2004PA001047, 2004.

Bradtmiller, L., Anderson, R., Fleisher, M., and Burckle, L.: Diatom productivity in the equatorial Pacific Ocean from the last glacial period to the present: A test of the silicic acid leakage hypothesis, Paleoceanography, 21, PA4201, https://doi.org/10.1029/2006PA001282, 2006.

Bradtmiller, L., Anderson, R., Fleisher, M., and Burckle, L.: Opal burial in the equatorial Atlantic Ocean over the last 30 ka: Implications for glacial-interglacial changes in the ocean silicon cycle, Paleoceanography, 22, PA4216,, https://doi.org/10.1029/2007PA001443, 2007.

Bradtmiller, L. I., Anderson, R. F., Fleisher, M. Q., and Burckle, L. H.: Comparing glacial and Holocene opal fluxes in the Pacific sector of the Southern Ocean, Paleoceanography, 24, PA2214, https://doi.org/10.1029/2008PA001693, 2009.

Brzezinski, M. A., Pride, C. J., Franck, V. M., Sigman, D. M., Sarmiento, J. L., Matsumoto, K., Gruber, N., Rau, G. H., and Coale, K. H.: A switch from $Si(OH)_4$ to NO_3^- depletion in the glacial Southern Ocean, Geophysical Research Letters, 29, 1564, https://doi.org/10.1029/2001GL014349, 2002.

Chase, Z., Anderson, R. F., Fleisher, M. Q., and Kubik, P. W.: Accumulation of biogenic and lithogenic material in the Pacific sector of the Southern Ocean during the past 40,000 years, Deep Sea Research Part II: Topical Studies in Oceanography, 50, 799–832, https://doi.org/10.1016/S0967-0645(02)00595-7, 2003.

Claquin, P., Martin-Jézéquel, V., Kromkamp, J. C., Veldhuis, M. J. W., and Kraay, G. W.: Uncoupling of Silicon Compared With Carbon and Nitrogen Metabolisms and the Role of the Cell Cycle in Continuous Cultures of Thalassiosira Pseudonana (Bacillariophyceae) Under

https://doi.org/10.5194/egusphere-2026-6527
Preprint. Discussion started: 4 November 2026
© Author(s) 2026. CC BY 4.0 License.

Light, Nitrogen, and Phosphorus Control, Journal of Phycology, 38, 922–930, https://doi.org/10.1046/j.1529-8817.2002.t01-1-01220.x, 2002.

Crosta, X., Beucher, C. P., Pahnke, K., and Brzezinski, M. A.: Silicic acid leakage from the Southern Ocean: Opposing effects of nutrient uptake and oceanic circulation, Geophysical research letters, 34, https://doi.org/10.1029/2006GL029083, 2007.

Danilov, S., Sidorenko, D., Wang, Q., and Jung, T.: The Finite-volumE Sea ice–Ocean Model (FESOM2), Geoscientific Model Development, 10, 765–789, https://doi.org/10.5194/gmd-10-765-2017, 2017.

de La Rocha, C. L., Brzezinski, M. A., DeNiro, M., and Shemesh, A.: Silicon-isotope composition of diatoms as an indicator of past oceanic change, Nature, 395, 680–683, https://doi.org/10.1038/27174, 1998.

Dubois, N., Kienast, M., Kienast, S., Calvert, S. E., François, R., and Anderson, R. F.: Sedimentary opal records in the eastern equatorial Pacific: It is not all about leakage, Global Biogeochemical Cycles, 24, GB4020, https://doi.org/10.1029/2010GB003821, 2010.

Dumont, M., Pichevin, L., Geibert, W., Crosta, X., Michel, E., Moreton, S., Dobby, K., and Ganeshram, R.: The nature of deep overturning and reconfigurations of the silicon cycle across the last deglaciation, Nature Communications, 11, 1534, https://doi.org/10.1038/s41467-020-15101-6, 2020.

Frank, M., Gersonde, R., van der Loeff, M. R., Bohrmann, G., Nürnberg, C. C., Kubik, P. W., Suter, M., and Mangini, A.: Similar glacial and interglacial export bioproductivity in the Atlantic Sector of the Southern Ocean: Multiproxy evidence and implications for glacial atmospheric CO2, Paleoceanography, 15, 642–658, https://doi.org/10.1029/2000PA000497, 2000.

Ganopolski, A. and Brovkin, V.: Simulation of climate, ice sheets and CO_2 evolution during the last four glacial cycles with an Earth system model of intermediate complexity, Climate of the Past, 13, 1695–1716, https://doi.org/10.5194/cp-13-1695-2017, 2017.

Garcia, H. E., Locarnini, R. A., Boyer, T. P., Antonov, J. I., Baranova, O. K., Zweng, M. M., Reagan, J. R., and Johnson, D. R.: World Ocean Atlas 2013, Volume 4: Dissolved Inorganic Nutrients (Phosphate, Nitrate, Silicate). S. Levitus, Ed., A. Mishonov Technical Ed., Tech. rep., NOAA Atlas NESDIS 76, 2014.

Garcia, H. E., Weathers, K. W., Paver, C. R., Smolyar, I., Boyer, T. P., Locarnini, R. A., Zweng, M. M., Mishonov, A. V., Baranova, O. K., Seidov, D., and Reagan, J. R.: World Ocean Atlas 2018, Volume 4: Dissolved Inorganic Nutrients (Phosphate, Nitrate, Silicate). A. Mishonov Technical Editor, Tech. rep., NOAA Atlas NESDIS 84, 2019.

Gu, S., Liu, Z., Zhang, J., Rempfer, J., Joos, F., and Oppo, D. W.: Coherent response of Antarctic Intermediate Water and Atlantic Meridional Overturning Circulation during the last deglaciation: reconciling contrasting neodymium isotope reconstructions from the tropical Atlantic, Paleoceanography, 32, 1036–1053, https://doi.org/10.1002/2017PA003092, 2017.

Gürses, O., Oziel, L., Karakuş, O., Sidorenko, D., Völker, C., Ye, Y., Zeising, M., Butzin, M., and Hauck, J.: Ocean biogeochemistry in the coupled ocean–sea ice–biogeochemistry model FESOM2.1–REcoM3, Geoscientific Model Development, 16, 4883–4936, https://doi.org/10.5194/gmd-16-4883-2023, 2023.

Hendry, K. R. and Brzezinski, M. A.: Using silicon isotopes to understand the role of the Southern Ocean in modern and ancient biogeochemistry and climate, Quaternary Science Reviews, 89, 13–26, https://doi.org/10.1016/j.quascirev.2014.01.019, 2014.

Hertzberg, J. E., Lund, D. C., Schmittner, A., and Skrivanek, A. L.: Evidence for a biological pump driver of atmospheric CO_2 rise during Heinrich Stadial 1, Geophysical Research Letters, 43, 12,242–12,251, https://doi.org/10.1002/2016GL070723, 2016.

Horn, M. G., Beucher, C. P., Robinson, R. S., and Brzezinski, M. A.: Southern ocean nitrogen and silicon dynamics during the last deglaciation, Earth and Planetary Science Letters, 310, 334–339, https://doi.org/10.1016/j.epsl.2011.08.016, 2011.

Huang, K.-F., Oppo, D. W., and Curry, W. B.: Decreased influence of Antarctic intermediate water in the tropical Atlantic during North Atlantic cold events, Earth and Planetary Science Letters, 389, 200–208, https://doi.org/10.1016/j.epsl.2013.12.037, 2014.

https://doi.org/10.5194/egusphere-2026-6527
Preprint. Discussion started: 4 November 2026
© Author(s) 2026. CC BY 4.0 License.

Kageyama, M., Albani, S., Braconnot, P., Harrison, S. P., Hopcroft, P. O., Ivanovic, R. F., Lambert, F., Marti, O., Peltier, W. R., Peterschmitt, J.-Y., Roche, D. M., Tarasov, L., Zhang, X., Brady, E. C., Haywood, A. M., LeGrande, A. N., Lunt, D. J., Mahowald, N. M., Mikolajewicz, U., Nisancioglu, K. H., Otto-Bliesner, B. L., Renssen, H., Tomas, R. A., Zhang, Q., Abe-Ouchi, A., Bartlein, P. J., Cao, J., Li, Q., Lohmann, G., Ohgaito, R., Shi, X., Volodin, E., Yoshida, K., Zhang, X., and Zheng, W.: The PMIP4 contribution to CMIP6 – Part 4: Scientific objectives and experimental design of the PMIP4-CMIP6 Last Glacial Maximum experiments and PMIP4 sensitivity experiments, Geoscientific Model Development, 10, 4035–4055, https://doi.org/10.5194/gmd-10-4035-2017, 2017.

Kageyama, M., Harrison, S. P., Kapsch, M.-L., Lofverstrom, M., Lora, J. M., Mikolajewicz, U., Sherriff-Tadano, S., Vadsaria, T., Abe-Ouchi, A., Bouttes, N., Chandan, D., Gregoire, L. J., Ivanovic, R. F., Izumi, K., LeGrande, A. N., Lhardy, F., Lohmann, G., Morozova, P. A., Ohgaito, R., Paul, A., Peltier, W. R., Poulsen, C. J., Quiquet, A., Roche, D. M., Shi, X., Tierney, J. E., Valdes, P. J., Volodin, E., and Zhu, J.: The PMIP4 Last Glacial Maximum experiments: preliminary results and comparison with the PMIP3 simulations, Climate of the Past, 17, 1065–1089, https://doi.org/10.5194/cp-17-1065-2021, 2021.

Kienast, S., Kienast, M., Jaccard, S., Calvert, S., and François, R.: Testing the silica leakage hypothesis with sedimentary opal records from the eastern equatorial Pacific over the last 150 kyrs, Geophysical Research Letters, 33, L15 607, https://doi.org/10.1029/2006GL026651, 2006.

Kohfeld, K. E. and Ridgwell, A.: Glacial-interglacial variability in atmopsheric CO_2, in: Surface Ocean–Lower Atmospheres Processes, edited by Saltzman, E. and Quéré, C. L., vol. 187 of *Geophysical Monograph Series*, pp. 251–286, AGU, Washington D.C., https://doi.org/10.1029/2008GM000845, 2009.

Kohfeld, K. E., Quéré, C. L., Harrison, S. P., and Anderson, R. F.: Role of Marine Biology in Glacial-Interglacial CO_2 Cycles, Science, 308, 74–78, https://doi.org/10.1126/science.1105375, 2005.

Kohfeld, K. E., Graham, R. M., De Boer, A. M., Sime, L. C., Wolff, E. W., Le Quéré, C., and Bopp, L.: Southern Hemisphere westerly wind changes during the Last Glacial Maximum: paleo-data synthesis, Quaternary Science Reviews, 68, 76–95, https://doi.org/10.1016/j.quascirev.2013.01.017, 2013.

Köhler, P. and Munhoven, G.: Late Pleistocene Carbon Cycle Revisited by Considering Solid Earth Processes, Paleoceanography and Paleoclimatology, 35, e2020PA004 020, https://doi.org/10.1029/2020PA004020, 2020.

Köhler, P., Skinner, L. C., and Adolphi, F.: Simulated radiocarbon cycle revisited by considering the bipolar seesaw and benthic ^{14}C data, Earth and Planetary Science Letters, 640, 118 801, https://doi.org/10.1016/j.epsl.2024.118801, 2024.

Koldunov, N. V., Aizinger, V., Rakowsky, N., Scholz, P., Sidorenko, D., Danilov, S., and Jung, T.: Scalability and some optimization of the Finite-volumE Sea ice–Ocean Model, Version 2.0 (FESOM2), Geoscientific Model Development, 12, 3991–4012, https://doi.org/10.5194/gmd-12-3991-2019, 2019.

Lauvset, S. K., Key, R. M., Olsen, A., van Heuven, S., Velo, A., Lin, X., Schirnick, C., Kozyr, A., Tanhua, T., Hoppema, M., Jutterström, S., Steinfeldt, R., Jeansson, E., Ishii, M., Perez, F. F., Suzuki, T., and Watelet, S.: A New Global Interior Ocean Mapped Climatology: The 1×1 GLODAP Version 2, Earth System Science Data, 8, 325–340, https://doi.org/10.5194/essd-8-325-2016, 2016.

Lippold, J., Luo, Y., Francois, R., Allen, S. E., Gherardi, J., Pichat, S., Hickey, B., and Schulz, H.: Strength and geometry of the glacial Atlantic Meridional Overturning Circulation, Nature Geoscience, 5, 813–816, https://doi.org/10.1038/ngeo1608, 2012.

Lippold, J., Pöppelmeier, F., Süfke, F., Gutjahr, M., Goepfert, T. J., Blaser, P., Friedrich, O., Link, J. M., Wacker, L., Rheinberger, S., et al.: Constraining the variability of the Atlantic meridional overturning circulation during the Holocene, Geophysical Research Letters, 46, 11 338–11 346, https://doi.org/10.1029/2019GL084988, 2019.

https://doi.org/10.5194/egusphere-2026-6527
Preprint. Discussion started: 4 November 2026
© Author(s) 2026. CC BY 4.0 License.

Marchetti, A. and Cassar, N.: Diatom elemental and morphological changes in response to iron limitation: a brief review with potential paleoceanographic applications, Geobiology, 7, 419–431, https://doi.org/10.1111/j.1472-4669.2009.00207.x, 2009.

Marchetti, A. and Harrison, P. J.: Coupled changes in the cell morphology and elemental (C, N, and Si) composition of the pennate diatom Pseudo-nitzschia due to iron deficiency, Limnology and Oceanography, 52, 2270–2284, https://doi.org/10.4319/lo.2007.52.5.2270, 2007.

Marcott, S. A., Bauska, T. K., Buizert, C., Steig, E. J., Rosen, J. L., Cuffey, K. M., Fudge, T., Severinghaus, J. P., Ahn, J., Kalk, M. L., et al.: Centennial-scale changes in the global carbon cycle during the last deglaciation, Nature, 514, 616–619, https://doi.org/10.1038/nature13799, 2014.

Matsumoto, K. and Sarmiento, J. L.: A corollary to the silicic acid leakage hypothesis, Paleoceanography, 23, PA2203, https://doi.org/10.1029/2007PA001515, 2008.

Matsumoto, K., Sarmiento, J. L., and Brzezinski, M. A.: Silicic acid leakage from the Southern Ocean: A possible explanation for glacial atmospheric pCO_2, Global Biogeochemical Cycles, 16, 1031, https://doi.org/10.1029/2001GB001442, 2002.

Pichevin, L. E., Reynolds, B. C., Ganeshram, R. S., Cacho, I., Pena, L., Keefe, K., and Ellam, R.: Enhanced carbon pump inferred from relaxation of nutrient limitation in the glacial ocean, Nature, 459, 1114–1117, https://doi.org/10.1038/nature08101, 2009.

Pöppelmeier, F., Jeltsch-Thömmes, A., Lippold, J., Joos, F., and Stocker, T. F.: Multi-proxy constraints on Atlantic circulation dynamics since the last ice age, Nature Geoscience, 16, 349–356, https://doi.org/10.1038/s41561-023-01140-3, 2023.

Raddatz, T. J., Reick, C., Knorr, W., Kattge, J., Roeckner, E., Schnur, R., Schnitzler, K.-G., Wetzel, P., and Jungclaus, J.: Will the tropical land biosphere dominate the climate–carbon cycle feedback during the twenty-first century?, Climate dynamics, 29, 565–574, https://doi.org/10.1007/s00382-007-0247-8, 2007.

Richaud, M., Loubere, P., Pichat, S., and Francois, R.: Changes in opal flux and the rain ratio during the last 50,000 years in the equatorial Pacific, Deep Sea Research Part II: Topical Studies in Oceanography, 54, 762–771, https://doi.org/10.1016/j.dsr2.2007.01.012, 2007.

Saini, H., Meissner, K. J., Menviel, L., and Kvale, K.: Transient Response of Southern Ocean Ecosystems During Heinrich Stadials, Paleoceanography and Paleoclimatology, 39, e2023PA004 754, https://doi.org/10.1029/2023PA004754, 2024.

Scholz, P., Sidorenko, D., Danilov, S., Wang, Q., Koldunov, N., Sein, D., and Jung, T.: Assessment of the Finite-VolumE Sea Ice–Ocean Model (FESOM2.0) – Part 2: Partial Bottom Cells, Embedded Sea Ice and Vertical Mixing Library CVMix, Geoscientific Model Development, 15, 335–363, https://doi.org/10.5194/gmd-15-335-2022, 2022.

Seltzer, A., Davidson, P., Shackleton, S., Nicholson, D., and Khatiwala, S.: Global ocean cooling of 2.3°C during the Last Glacial Maximum, Geophysical Research Letters, 51, e2024GL108 866, https://doi.org/10.1029/2024GL108866, 2024.

Shi, X., Cauquoin, A., Lohmann, G., Jonkers, L., Wang, Q., Yang, H., Sun, Y., and Werner, M.: Simulated stable water isotopes during the mid-Holocene and pre-industrial using AWI-ESM-2.1-wiso, Geoscientific Model Development Discussions, 2023, 1–39, https://doi.org/10.5194/gmd-2023-68, 2023.

Shi, X., Werner, M., Pausata, F. S. R., Liu, J., D'Agostino, R., Hu, Y., Yang, H., Wang, H., Yang, C., and Lohmann, G.: Climate-Dependency of Impact of Increased Carbon Dioxide on African Monsoon Rainfall: Insights From Model Simulations, Geophysical Research Letters, 52, e2024GL112 717, https://doi.org/10.1029/2024GL112717, 2025.

Sidorenko, D., Goessling, H., Koldunov, N., Scholz, P., Danilov, S., Barbi, D., Cabos, W., Gurses, O., Harig, S., Hinrichs, C., Juricke, S., Lohmann, G., Losch, M., Mu, L., Rackow, T., Rakowsky, N., Sein, D., Semmler, T., Shi, X., Stepanek, C., Streffing, J., Wang, Q., Wekerle, C., Yang, H., and Jung, T.: Evaluation of FESOM2.0 Coupled to ECHAM6.3: Preindustrial and HighResMIP Simulations, Journal of Advances in Modeling Earth Systems, 11, 3794–3815, https://doi.org/10.1029/2019MS001696, 2019.

https://doi.org/10.5194/egusphere-2026-6527
Preprint. Discussion started: 4 November 2026
© Author(s) 2026. CC BY 4.0 License.

Sigman, D. M., Fripiat, F., Studer, A. S., Kemeny, P. C., Martínez-García, A., Hain, M. P., Ai, X., Wang, X., Ren, H., and Haug, G. H.: The Southern Ocean during the ice ages: A review of the Antarctic surface isolation hypothesis, with comparison to the North Pacific, Quaternary Science Reviews, 254, 106 732, https://doi.org/10.1016/j.quascirev.2020.106732, 2021.

Skinner, L., Primeau, F., Jeltsch-Thömmes, A., Joos, F., Köhler, P., and Bard, E.: Rejuvenating the ocean: mean ocean radiocarbon, CO_2 release, and radiocarbon budget closure across the last deglaciation, Climate of the Past, 19, 2177–2202, https://doi.org/10.5194/cp-19-2177-2023, 2023.

Steele, M., Morley, R., and Ermold, W.: PHC: A Global Ocean Hydrography with a High-Quality Arctic Ocean, Journal of Climate, 14, 2079–2087, https://doi.org/10.1175/1520-0442(2001)014<2079:PAGOHW>2.0.CO;2, 2001.

Stevens, B., Giorgetta, M., Esch, M., Mauritsen, T., Crueger, T., Rast, S., Salzmann, M., Schmidt, H., Bader, J., Block, K., Brokopf, R., Fast, I., Kinne, S., Kornblueh, L., Lohmann, U., Pincus, R., Reichler, T., and Roeckner, E.: Atmospheric component of the MPI-M Earth System Model: ECHAM6, Journal of Advances in Modeling Earth Systems, 5, 146–172, https://doi.org/10.1002/jame.20015, 2013.

Stocker, T. F. and Johnsen, S. J.: A minimum thermodynamic model for the bipolar seesaw, Paleoceanography, 18, 1087, https://doi.org/10.1029/2003PA000920, 2003.

Takeda, S.: Influence of iron availability on nutrient consumption ratio of diatoms in oceanic waters, Nature, 393, 774–777, https://doi.org/10.1038/31674, 1998.

Tarasov, L., Dyke, A. S., Neal, R. M., and Peltier, W.: A data-calibrated distribution of deglacial chronologies for the North American ice complex from glaciological modeling, Earth and Planetary Science Letters, 315-316, 30 – 40, https://doi.org/10.1016/j.epsl.2011.09.010, 2012.

Tierney, J. E., Zhu, J., King, J., Malevich, S. B., Hakim, G. J., and Poulsen, C. J.: Glacial cooling and climate sensitivity revisited, Nature, 584, 569–573, https://doi.org/10.1038/s41586-020-2617-x, 2020.

Tréguer, P. J. and De La Rocha, C. L.: The World Ocean Silica Cycle, Annual Review of Marine Science, 5, 477–501, https://doi.org/10.1146/annurev-marine-121211-172346, 2013.

Tréguer, P. J., Sutton, J. N., Brzezinski, M., Charette, M. A., Devries, T., Dutkiewicz, S., Ehlert, C., Hawkings, J., Leynaert, A., Liu, S. M., Llopis Monferrer, N., López-Acosta, M., Maldonado, M., Rahman, S., Ran, L., and Rouxel, O.: Reviews and Syntheses: The Biogeochemical Cycle of Silicon in the Modern Ocean, Biogeosciences, 18, 1269–1289, https://doi.org/10.5194/bg-18-1269-2021, 2021.

Waelbroeck, C., Paul, A., Kucera, M., Rosell-Melé, A., Weinelt, M., R. Schneiderand A. C. Mix, A. Abelmann, L. A., Bard, E., Barker, S., Barrows, T. T., Benway, H., Cacho, I., Chen, M.-T., Cortijo, E., Crosta, X., de Vernal, A., Dokken, T., Duprat, J., Elderfield, H., Eynaud, F., Gersonde, R., Hayes, A., Henry, M., Hillaire-Marcel, C., Huang, C.-C., Jansen, E., Juggins, S., Kallel, N., Kiefer, T., Kienast, M., Labeyrie, L., Leclaire, H., Londeix, L., Mangin, S., Matthiessen, J., Marret, F., Meland, M., Morey, A. E., Mulitza, S., Pflaumann, U., Pisias, N. G., Radi, T., Rochon, A., Rohling, E. J., Sbaffi, L., Schäfer-Neth, C., Solignac, S., H. Spero, K. T., and Turon, J.-L.: Constraints on the magnitude and patterns of ocean cooling at the Last Glacial Maximum, Nature Geoscience, 2, 127–132, https://doi.org/10.1038/ngeo411, 2009.

Wu, J., Mollenhauer, G., Stein, R., Köhler, P., Hefter, J., Fahl, K., Grotheer, H., Wei, B., and Nam, S.-I.: Deglacial release of petrogenic and permafrost carbon from the Canadian Arctic impacting the carbon cycle, Nature Communications, 13, 7172, https://doi.org/10.1038/s41467-022-34725-4, 2022.

Ye, Y.: Ocean biogeochemistry model FESOM2.1-REcoM3 coupled with a sediment model MEDUSA2, Zenodo [software], https://doi.org/10.5281/zenodo.8315239, 2023.

https://doi.org/10.5194/egusphere-2026-6527
Preprint. Discussion started: 4 November 2026
© Author(s) 2026. CC BY 4.0 License.



Ye, Y., Munhoven, G., Köhler, P., Butzin, M., Hauck, J., Gürses, Ö., and Völker, C.: FESOM2.1-REcoM3-MEDUSA2: an ocean–sea ice–
580 biogeochemistry model coupled to a sediment model, Geoscientific Model Development, 18, 977–1000, https://doi.org/10.5194/gmd-18-977-2025, 2025.